# THIN-FILM INTRACORTICAL RECORDING MICROELECTRODES

## Quarterly Report #6

(Contract NIH-NINDS-NO1-NS-0-2329)

### *January – March 2002*

Submitted to the

### *Neural Prosthesis Program*
National Institute of Neurological Disorders and Stroke
National Institutes of Health

by the

## Center for Wireless Integrated MicroSystems
Department of Electrical Engineering and Computer Science
The University of Michigan
Ann Arbor, Michigan
48109-2122

April 2002

# Thin-Film Intracortical
# Recording Microelectrodes

## *Summary*

During the past quarter, research has moved forward in a number of areas.  We are using immunocytochemical methods to study the sheath that forms around chronic recording electrodes and have identified two or three cellular components to this envelope.  The inner layer is made up of epithelial cells, followed by reactive glia (astrocytes).  A third component, neuronal processes, is less consistently present. Understanding these components should help us develop probes that are able to record consistently over much longer periods of time.  We are also continuing to explore the use of liquid-crystal polymer (LCP) for the formation of flexible microcables for in-vivo use. The cables under test are 8cm long.  Working with Dr. David Edell, we have insulated these cables with silicone and are soak testing the probes in-vitro.  After more than three months, the cables are still exhibiting very high resistances against site-site leakage.

Both trench-refill boron-diffusion-based probe technology and silicon-on-insulator approaches are being explored as possible alternatives to the present boron-diffused process for probe fabrication.  Although no substantial performance advantages associated with the new processes are seen at this time, probes are being fabricated with both approaches to ensure that the most appropriate approach to probe fabrication is being pursued.

Active probes are being used in-vivo for current source density measurements by Dr. Gyorgy Buzsaki at Rutgers University.  The 12-16-site buffered active probes have shown much superior performance with regard to immunity from motion artifact as compared to passive probes.  They also eliminate the need for a headstage, simplifying the capture of multi-channel recordings.  Sixty-four-site non-multiplexed probes  (Pia-2B) are also being used to record from hippocampal single units with very good results. Multiplexed 64-site active probes (Pia-2) are being used in-vivo at Michigan, where software is being developed to allow multiplexed data acquisition and use of the front-end selector.   The capacitively-coupled amplifiers used on these probes provide a per-channel gain of 100 and a bandwidth from <10Hz to >40kHz.  The amplifiers provide a stable DC baseline and freedom from optical offsets.  We are moving toward completion of a platform-mounted signal processing chip that will allow the recorded spikes to be digitized and then passed to the external world, eliminating the considerable bandwidth that would otherwise be used in transmitting below-threshold noise.  A 5b analog-to-digital converter is being designed as part of the processing chip.  We expect this chip to be fabricated during the coming term using the MOSIS foundry.

Finally, we have designed an external transmitter to provide power and command signals to the implanted probes.  This circuitry was fully implemented and was used to

provide data using a 4MHz carrier. Data rates were as high as 60kbps. An active on-chip transmitter was also designed for use on the platform. This transmitter is designed to work at 100MHz with a bit rate of 10MHz. Power consumption levels for the transmitter are about 2mW.

# Thin-Film Intracortical Recording Microelectrodes

## 1.  Introduction

The goal of this program is the realization of batch-fabricated recording electrode arrays capable of accurately sampling single-unit neural activity throughout of volume of cortical tissue on a chronic basis.  Such arrays will constitute an important advance in instrumentation for the study of information processing in neural structures and should be valuable for a number of next-generation closed-loop neural prostheses, where stimuli must be conditioned on the response of the physiological system.

The approach taken in this research involves the use of solid-state process technology to realize probes in which a precisely-etched silicon substrate supports an array of thin-film conductors insulated above and below by deposited dielectrics. Openings in the dielectrics, produced using photolithography, form recording sites which permit recording from single neurons on a highly-selective basis.  The fabrication processes for both passive and active (containing signal-processing circuitry) probe structures have been reported in the past along with scaling limits and the results of numerous acute experiments using passive probes in animals.  In moving to chronic implant applications, the major problems are associated with the preserving the viability of the sites in-vivo (preventing tissue encapsulation of the sites) and with the probe output leads, both in terms of their number and their insulation.  The probe must float in the tissue with minimal tethering forces, limiting the number of leads to a few at most. The encapsulation of these leads must offer adequate protection for the megohm impedance levels of the sites while maintaining mechanical lead flexibility.

Our solution to the lead problem has involved two steps.  The first has been to embed circuitry in the probe substrate to amplify and buffer the signals and to multiplex them onto a common output line.  Using this approach, signal levels are increased by factors of over 100, impedance levels are reduced by three to four orders of magnitude, and the probe requires only a few leads for operation, independent of the number of recording sites.  A high-yield merged process permitting the integration of CMOS circuitry on the probe has been developed, and this circuitry has been designed and characterized.  The second step has involved the development of silicon-based ribbon cables, realized using the same probe technology, to conduct the neural signals to the outside world.  These cables have shown significant advantages over discrete leads, both in terms of the ease with which chronic implants can be assembled and in terms of the ability of the cables to survive long-term biased soaks in saline.  The cables can be built directly into the probes so that they come off of the wafer as a single unit, requiring no joining or bonding operations between them.  The cables are also significantly more flexible than previously-used discrete wire interconnects.

This contract calls for the development of active probes for neural recording.  A 64-site 8-channel probe with site selection and signal buffering but no multiplexing has

been developed (PIA-2B) along with a high-end multiplexed probe that includes gain (PIA-2).  These probes are now being refined and applied to in-vivo applications.  Investigations are on-going to better understand site encapsulation, which limits the lifetime of chronic recording structures, and telemetry is being developed to allow the probes to be operated over a wireless link, eliminating the percutaneous connector.

During the past quarter, we have continued work on understanding the chronic recording performance of the probes, on exploring alternative fabrication processes for them, and on using active probes in-vivo. We are also completing work on platform-mounted spike recognition circuitry for the probes as well as a wireless interface for them.  Work in these areas is discussed in the sections below.

## 2.  Chronic Studies with Passive Recording Probes

In conjunction with the Center for Neural Communication Technology (CNCT), we have been using immunocytochemical methods to differentiate the components of the cellular envelope surrounding the electrode tracts in chronically implanted guinea pigs.  We find that there are 2-3 cellular components to this envelope.  The innermost layer is a consistent component, made up of epithelial cells, further differentiated as epithelial cells of meningeal origin (meningeal fibrocytes) based on immunostaining for the intermediate filament vimentin (Fig. 1a).  A second consistent layer is identified as reactive glia (astrocytes), based on immunostaining for the intermediate filament glial fibrillary acid protein (Fig. 1b). This appears to be the second layer of the cellular envelope.
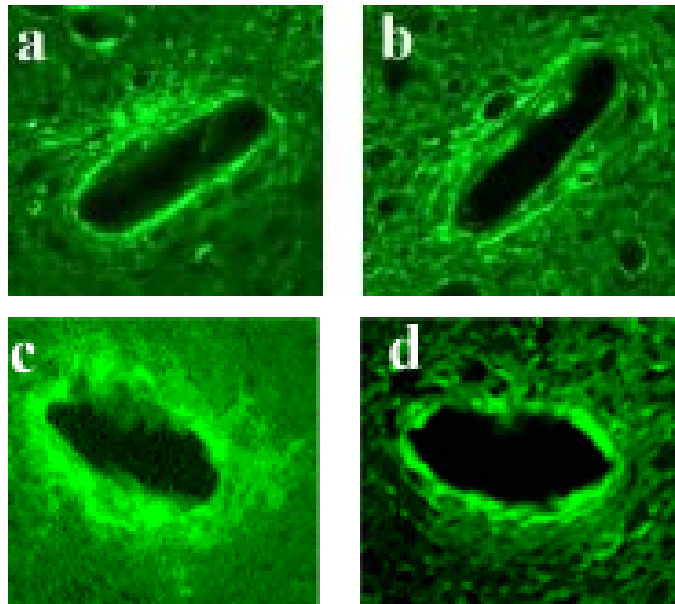


Fig. 1:  Immonuhistochemical staining of the neural tissue surrounding an implanted electrode.  a)intermediate filament vimentin  b)GFAP  c)fibronectin  d)vimentin

A third cellular component, neuronal processes, differentiated by immunostaining for the intermediate filaments neurofilament 150 or neurofilament 200, is less consistently present.  The presence varies not only among probe tracts but even along the length of a probe tract.   Fibronectin immunostaining is often seen adjacent to the neuroprobe tract (Fig. 1c), suggesting the fibrocytes are secreting this epithelial related extracellular matrix (ECM) that is often associated with wound healing.  Occassionally fibronectin will form a "path" away from the probe tract, suggesting migration had taken place.

Immunostaining for vimentin, the ECM associated with neurons, has a more variable presence in association with probe tracts, consistent with the variability seen in neuronal processes in the tissue envelope (Fig. 1d).  We are now examining changes in the cellular envelope over time, examining earlier time points following probe placement.  We will also compare the size of the cellular envelope and its components at different times and make comparisons to probe performance.

One of the important parts of this research is learning how to optimize the chronic recording capabilities of these probes, and that depends critically on packaging.  During the past quarter we encountered problems with the packaging of the chronic 32-channel electrode placed in guinea pig inferior colliculus.  These problems led to breakage during implantation and movement of the electrode once implanted.   We are currently in the process of redesigning the way it is packaged and expect the redesigned probe to function well on a chronic basis in terms of its packaging.

## 3. Packaging Developments

We are continuing to explore LCP (liquid crystal polymer) as one material for a flexible microcable to mate to the probe.  As required by the statement of work, this cable must be at least 2cm in length and the 4mm closest to the probe should be as flexible as a 100μm diameter gold wire.  As shown in Fig. 2, we are exploring a hybrid system with an integrated silicon cable forming the first 4mm portion and a more robust cable (such as LCP) forming the secondary portion of the interconnect.

As described in Quarterly Report #2 for this contract, we are working with LCP cables from Foster-Miller, Inc. of Waltham, MA.  They have fabricated both 1 and 2 mil thick cables with lengths ranging from 2 to 9cm.  The leads are made from thin layers of gold and nickel over copper foil.  The pitch on the cables is 6 mils to match the pitch of the standard probe bonding pads.  While the current LCP cables have no upper layer to insulate the leads, Foster-Miller is developing methods to apply a top LCP layer for passivation.  In the interim, we are working with Dr. David Edell of InnerSea Technology to coat the cables with silicone for insulation.

Soak tests are being performed by Dr. Edell to determine the viability of silicone as an insulator for these devices.  Soak test probes (probes that have no recording site vias opened through the top dielectrics) were ultrasonically bonded with aluminum wire

to 8cm long LCP cables and sent to InnerSea Technology for coating and attachment of the connector using a solder reflow process. The wire bond area of the device, the conductors on the LCP cable, and the connector solder joints were insulated with Nusil MED4-4220 silicone. The entire assembly, including the soldered connections, was put under bias in a 37° saline soak (Fig. 3). As shown in Fig. 4, after over 3 months the structure is still exhibiting stable, high sheet resistance ($>1x10^{15}$ohms/square). This is an important finding since, as described by Dr. Edell, silicones are the only encapsulant yet identified that protect silicon probe surfaces for at least 14 years.
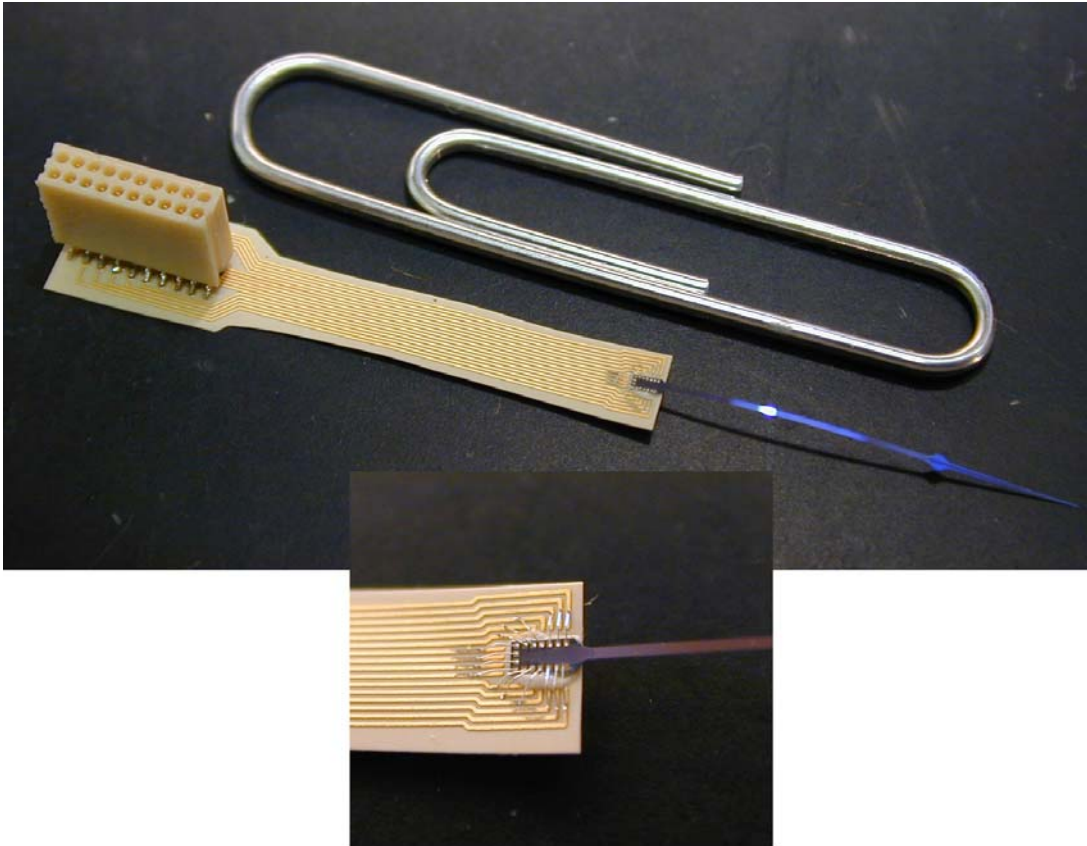


Fig. 2: Hybrid chronic assembly constructed from an integrated silicon cable/probe, an intermediate LCP cable, and a surface-mount Omnetics NANO connector. The total length of this structure, shown beside a standard paper clip, is 4cm from the tip of the probe to the back edge of the connector. Electrical connection between the silicon and LCP devices was accomplished using ultrasonic bonding.

Fig. 3:  Underside of a soak test jar top showing the LCP-silicon probe assembly with an 8cm long LCP interconnect cable.  The cable is folded back on itself to protect silicon probe from sides of soak jar.  Note that all connections are under soak in this assembly (wire bonds, gold/copper traces and solder joints at connector). *Photo courtesy of Dr. David Edell.*
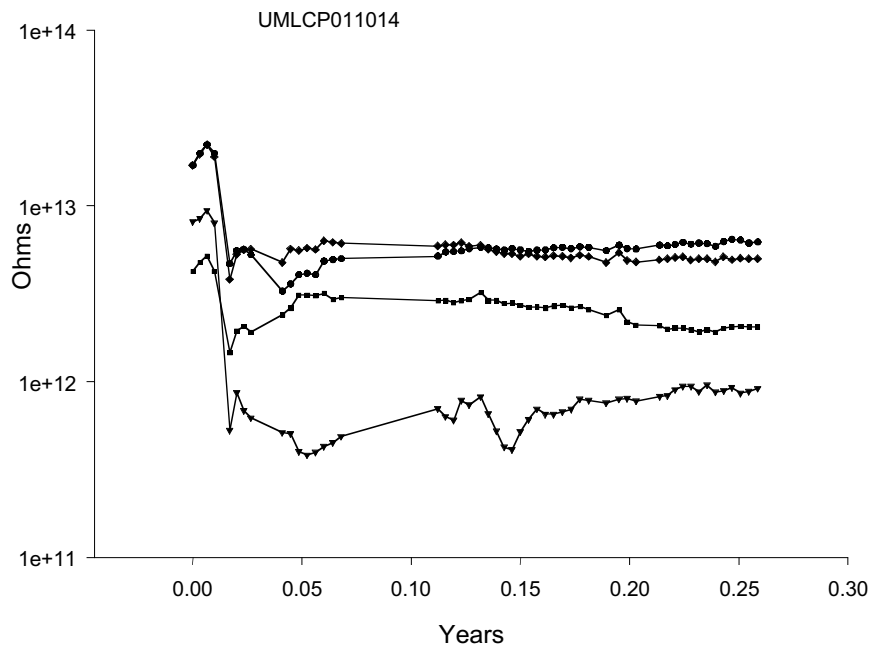


Fig. 4:  Early results of an LCP cable assembly soak test.  The assembly was encapsulated with silicone and placed in saline soak.  Traces are leakage current between adjacent sets of interconnect traces. *Data courtesy of Dr. David Edell.*

## 4. Scaled Recording Probe Development

Recording studies call for an increasing number of sites, and to minimize the tissue trauma associated with array insertion and residence, it is important that the shanks be as small as possible. In the past, we have demonstrated that shanks can be made much narrower than our standard dimensions (50-80µm), and we are now developing techniques for the reducing shank width considerably. Such "nanoprobes" should minimize tissue damage, allowing recordings from multiple sites within the field of a single cell as well as the transparent spacing of sites throughout a block of relatively-undisturbed neural tissue. We also want to look at all alternative processes to ensure we the process we are using is the best available for these sorts of devices. The process demonstrated in the past extends the field dielectric etch to countersink the substrate silicon, thus trimming the lateral extent of the boron diffusion and resulting in probe shanks as narrow as 5µm. This, however, limits the recording site to the narrow shank. We are interested in realizing sites that overhang the substrate, allowing a low impedance sites and a more spherical recording field. The competing technologies are a trench-refill approach, which extends the present process, and an silicon-on-insulator (SOI) approach, that results in a dielectric etch-stop all around the probe.

In the trench refill process, shown in the last quarterly report, a high-aspect-ratio trench is etched and then refilled with polysilicon so that the substrate boron diffusion is trimmed but the field area can still be planarized for further lithographic processing. The sites can then be formed and the probe then released using the usual techniques. The process adds one mask to the normal probe process and is compatible with the very smooth tip formation characteristic of our standard process. The sidewalls are chisel-shaped behind the tip.

In the SOI approach, a bond-and-etch-back wafer is used with a 10-15µm-thick silicon layer on top of oxide. High-aspect-ratio trenches are etched and refilled with dielectric in the shape of the probe. The normal probe processing then moves forward, excluding any boron diffusions for shank formation. Following circuit and site formation, the probes are released from the wafer using a bulk silicon etch as now. This approach uses a lightly doped silicon substrate that is naturally circuit compatible and yet it achieves a dielectric wall all around the probe. However, the bottom dielectric is cannot normally be specified and stress compensation in this structure may be difficult. In addition, it is likely that the lightly doped shanks will give rise to considerably more optical noise than the current structures. If the boron diffusions now used were more standard in the MEMS industry (and we continue to feel they will become so), then we suspect the present process would still be preferred. But we are exploring the SOI approach to understand it more fully and allow direct comparison. SOI material availability is certainly one issue since this is not the normal SOI material that will be used widely for submicron VLSI circuits.

During the coming term we plan to fabricate probes using both of the new processes and then make a decision regarding whether to continue pursuing either of these alternatives to the present structure.

# 5. Characterization of Non-Multiplexed Recording Probes

## 5.1 Active Probe In-vivo Characterization and Testing

During the past quarter, collaboration with Rutgers University in the characterization and in-vivo testing of active probes has continued. Several designs of 12-16 channel probes with on-chip buffering have been evaluated, and comparisons have been made to otherwise identical passive probes. In addition, experimental work has also been carried out during the past quarter with active 64-site buffered probes; some results from these experiments are presented in the next section.

Extensive data have been collected over the past years in Gyurgy Buzsaki's laboratory with so-called tetrode probes: 12-16 site passive probes with 2-4 shanks and closely-spaced (~20μm) sites. One problem noted with these probes has been the electrode sensitivity to motion. In chronic recording situations, an animal may be free to move around in its environment, and small bumps and movements are common. In addition, the animal will often groom itself, all of which will couple charge into the electrodes and result in large voltage transients. Motion artifact has been a severe constraint limiting experiments with awake, behaving animals. It has been suggested that on-chip buffering would shorten the length of the high impedance input node and thus decrease the incidence of charge coupled into the input. To test this hypothesis, probes identical to several in common use at Rutgers were fabricated with on chip buffering. Motion sensitivity was evaluated both by tapping the micromanipulator holding the electrode, and by waving a hand immediately above the electrode (thought to induce movement through the movement of air.) In both cases, the probe was inserted into rat cortex. For the passive probe, a commercially-available unity-gain headstage amplifier was used to buffer the signal before sending it to a data acquisition system. In the case of the active probe, no headstage amplifier was used, and the probe alone drove 6-10 feet of shielded cable to a breakout box connecting it to the data acquisition system.
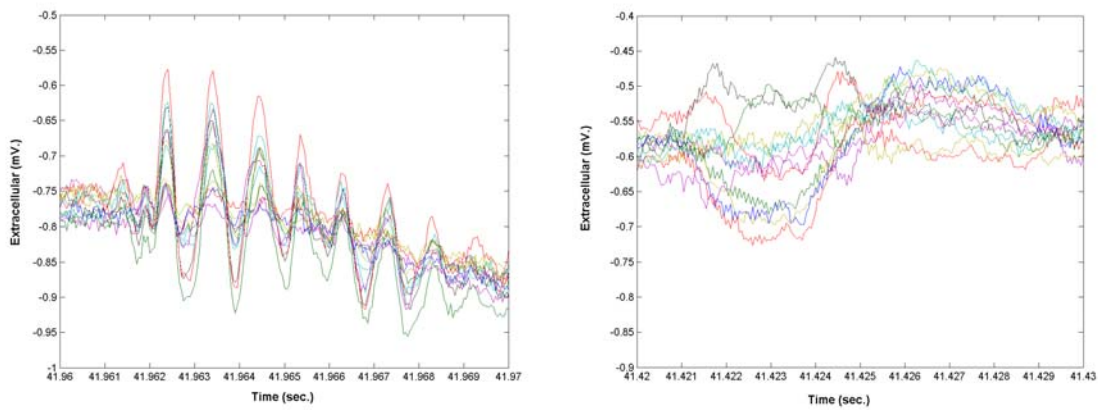


Fig. 5: Neural probe response to manual tapping of micromanipulator probe
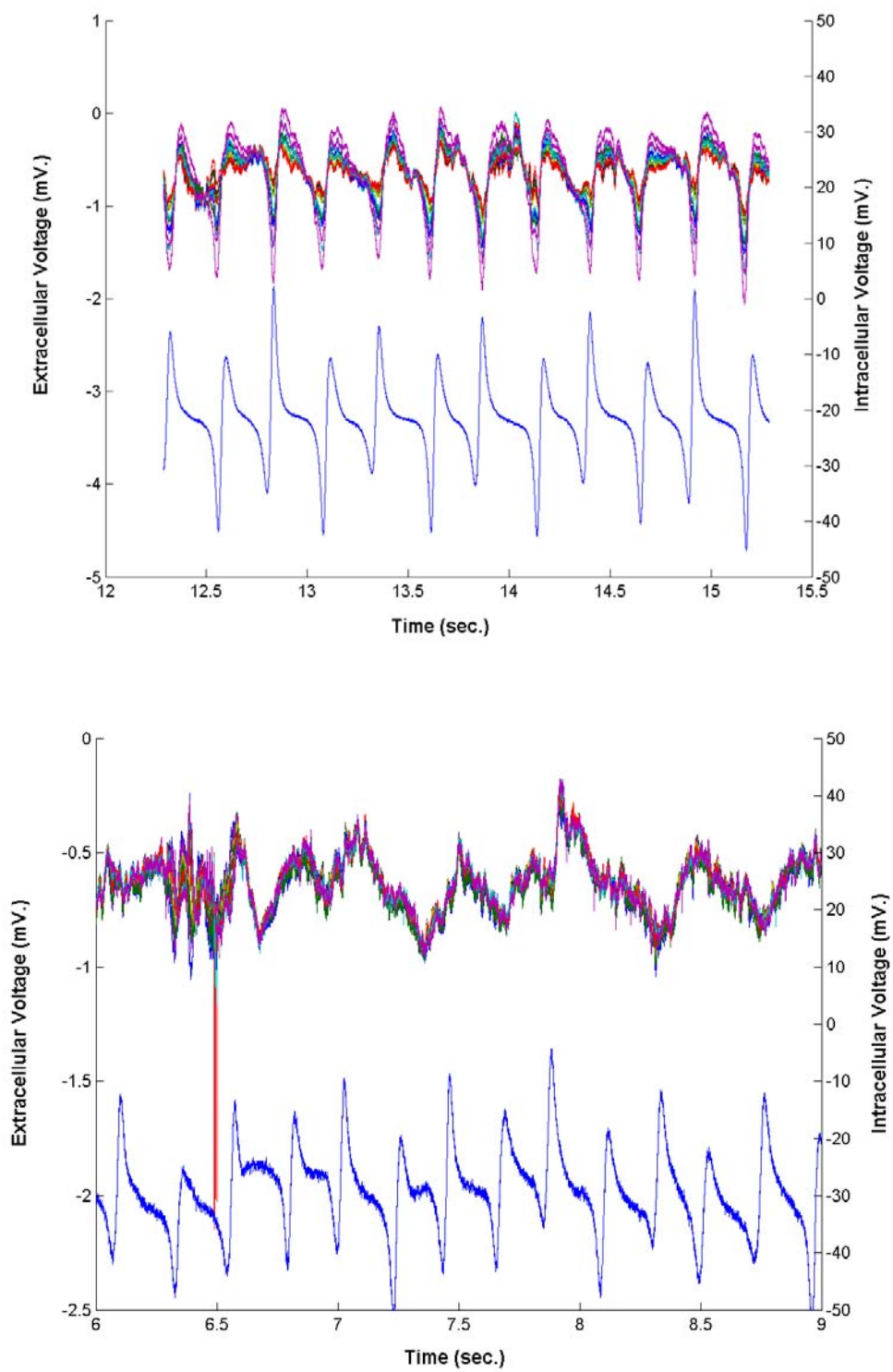without (left) and with (right) on-chip buffering.

Fig. 6: Passive probe (top trace in top figure) and active probe(top trace in bottom figure) response to waving hand above site of electrode penetration. Lower trace indicates timing of hand wave (see text for explanation.)

The resulting comparisons between probes with and without on-chip buffering are shown in Figs. 5 and 6. Data from all twelve channels are superimposed in the figure. The vertical and horizontal scales are identical in each case. The data in Fig. 5 has been filtered from 1Hz to 10kHz. Both probes are inserted in rat cortex; aside from the buffering they are identical. In Fig. 6, the lower trace is from an intracellular electrode inserted simultaneously with the probe. Because this electrode is highly sensitive to motion artifact, it serves as a useful marker for the timing of the hand waving. This data is also filtered from 1Hz. to 10kHz. It can be seen that in both the tapping and waving experiments, on-chip buffering greatly reduces motion artifact. There is significant inter-channel variability in motion sensitivity in both the active and passive case; the cause is unknown.

The data is even more striking after filtering, as is typically done for discriminating action potentials. In Fig. 7, data from a single channel of a passive and active probe during the tapping test is shown. This data has been filtered from 200Hz to 10kHz. The timing of micromanipulator taps is indicated by the vertical bars at the bottom of the figure. In the case of the passive probes the resulting spikes are very large and dwarf what appears to be normal action potentials in the period between taps. In the active case, evidence of transients locked to the tap frequency is visible, but the response is an order of magnitude smaller. The two large spikes in this trace occur at times approximately 5msec before and after a tap, and they are clearly physiological in nature (see inset at bottom.) By contrast, the tap-induced spikes in the top trace are clearly not physiological, showing evidence of the ringing we would expect from the motion of the micromanipulator after being tapped.

Figures 8-11 show data collected using twelve-site active tetrodes in experiments previously performed with passive tetrodes. Data was filtered from 1Hz to 10kHz so that information about both field and single unit activity could be extracted. A large spontaneous spike can be seen in Fig. 8; the details of the spike waveform are shown in Fig. 9. Due to the close site spacing, the spikes are recorded simultaneously on all four of the sites on a single shank. The simultaneously recorded waveforms can be used to perform more accurate spike sorting. Fig. 10 shows the wideband response of a single shank in the CA1 region of hippocampus during a sharp wave. Evidence of high frequency ripple during the sharp wave is clearly evident; it is the oscillation with a period of roughly 10msec evident on all four channels that begins at roughly 9.9 seconds. Three of the five large spikes are locked to the negative phase of the ripple, as expected. The filtered data in Fig. 11 shows the large spikes and excellent signal-to-noise ratio during this experiment.

Experiments are planned in the next quarter that will utilize these small active tetrodes implanted into rat hippocampus for periods of several weeks, attempting to obtain recordings from the animals while they are awake and behaving. In the next quarter we will also report the results of chronic in-vitro soak tests of active probes, which are ongoing.
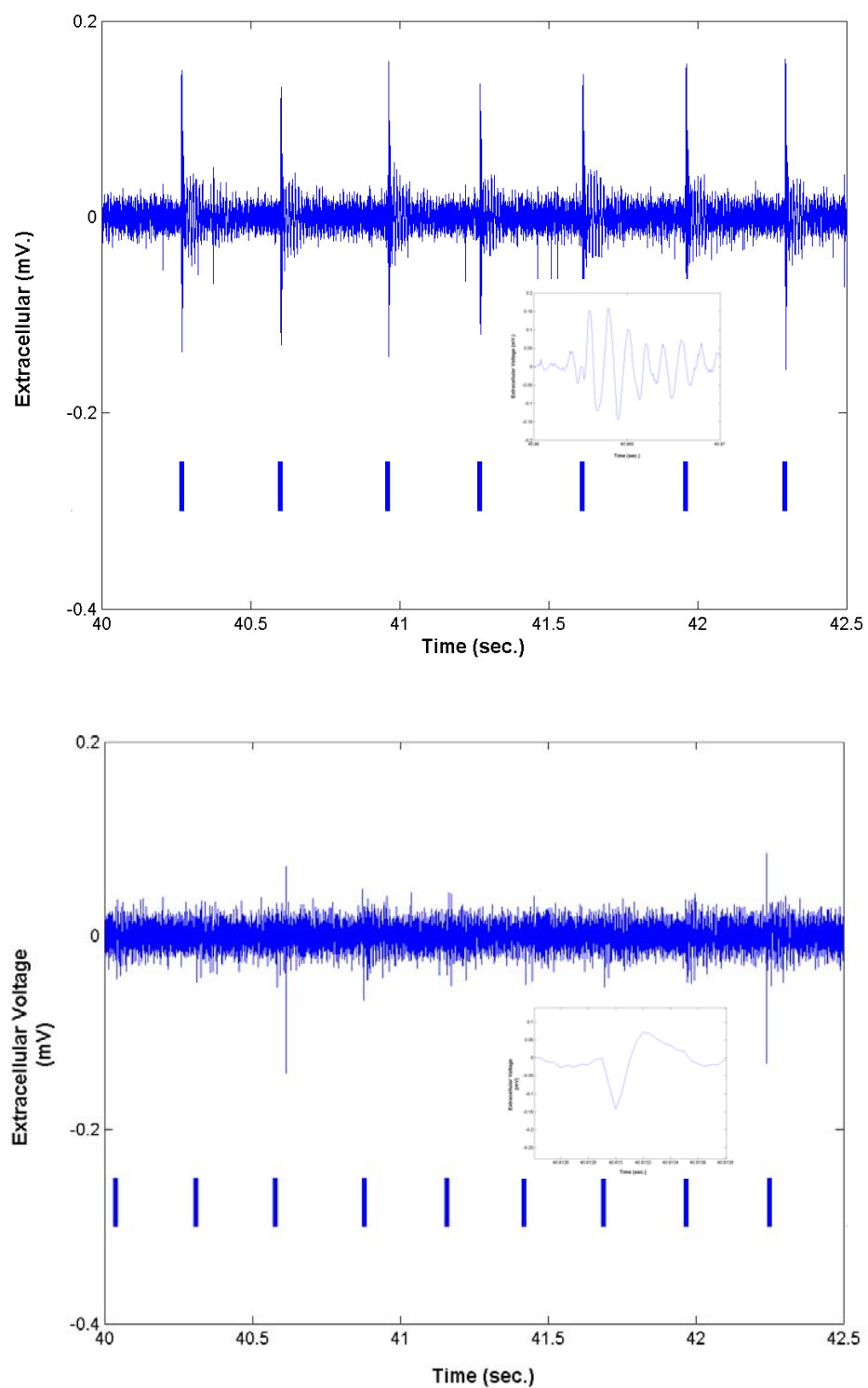
Fig. 3: Single channel response of a passive probe (top)
and a probe with on-chip buffer (bottom) to periodic tapping of micromanipulator. Insets
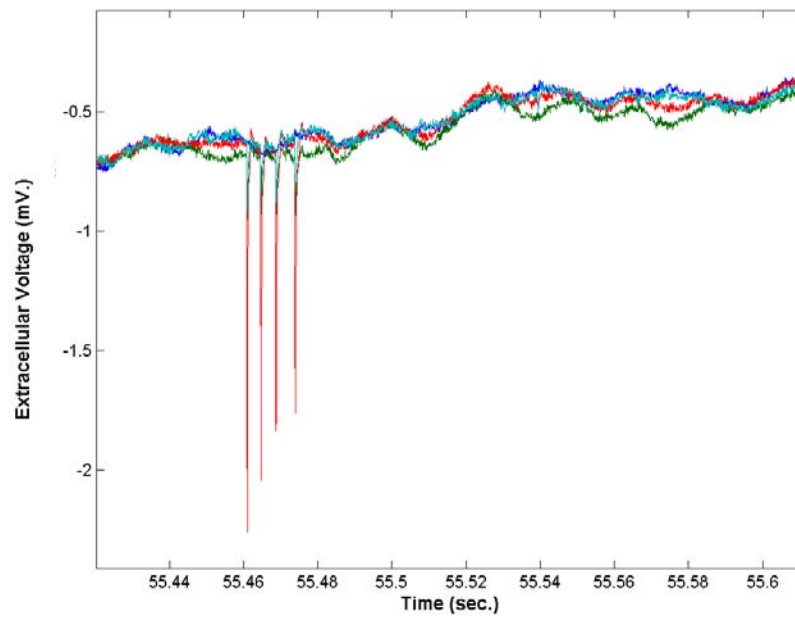show details of spikes in each case.

Fig. 8: Wideband recording from a tetrode on a twelve site probe with on-chip buffering. Large spontaneous action potentials are evident.
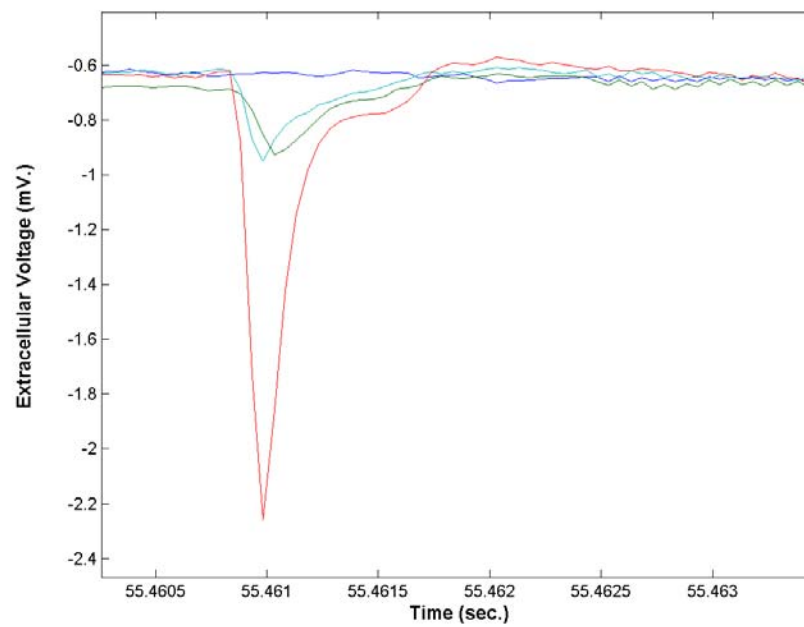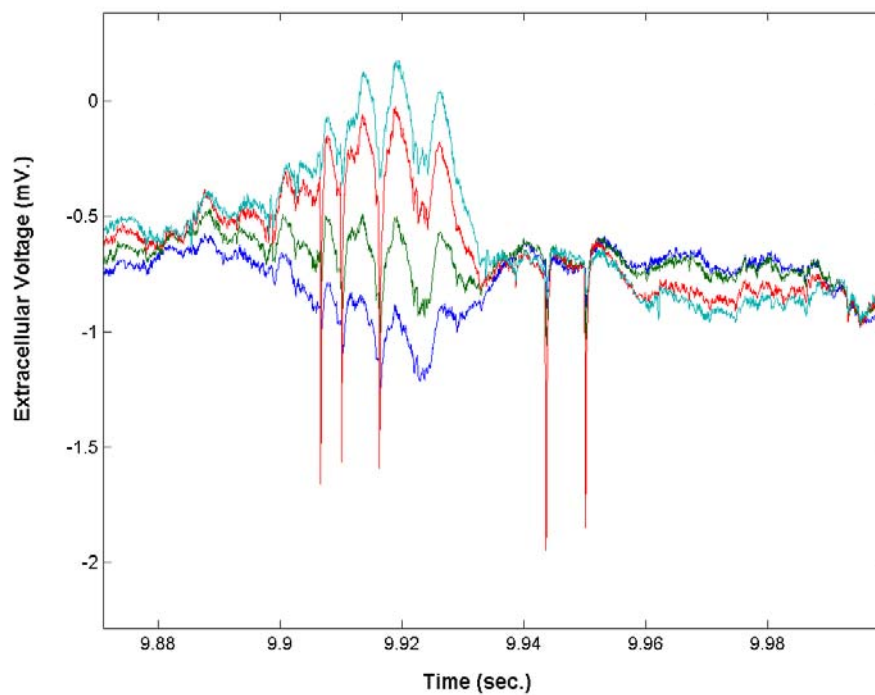


Fig. 9: Details of spike waveforms on all channels.

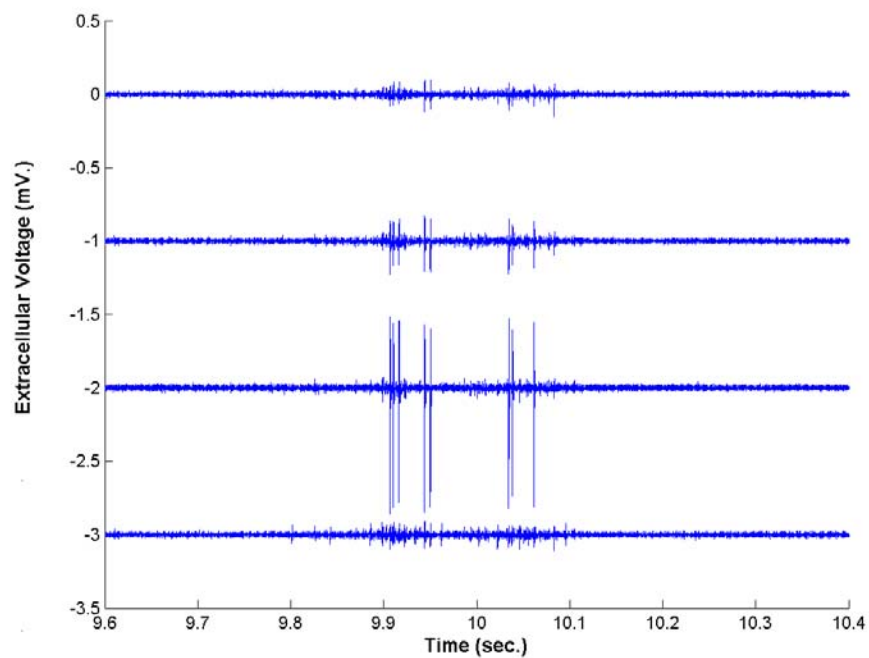Fig. 10: Wideband recording with active tetrode in CA1 during hippocampal sharp wave.



Fig. 11: Filtered (200Hz to 10kHz.) version of data in Fig. 10.

15

### *5.2 Recordings with 64 Site Buffered Probes*

Following the characterization and testing of the active tetrodes described above, experiments were begun with an active 64-site probe that was designed for high density recording of hippocampal single units. The design features eight shanks with eight closely spaced sites on each; all sixty-four channels are buffered with a unity gain op-amps. The inclusion of on-chip buffering, besides having the benefits discussed above, greatly simplifies the experimental set-up by eliminating the need for a headstage amplifier. Data from the buffered probe is sent directly out over ten-foot serial cables to a rack-mounted Sensorium amplifier. Some initial data obtained in these experiments is presented below in Figs. 12-14.
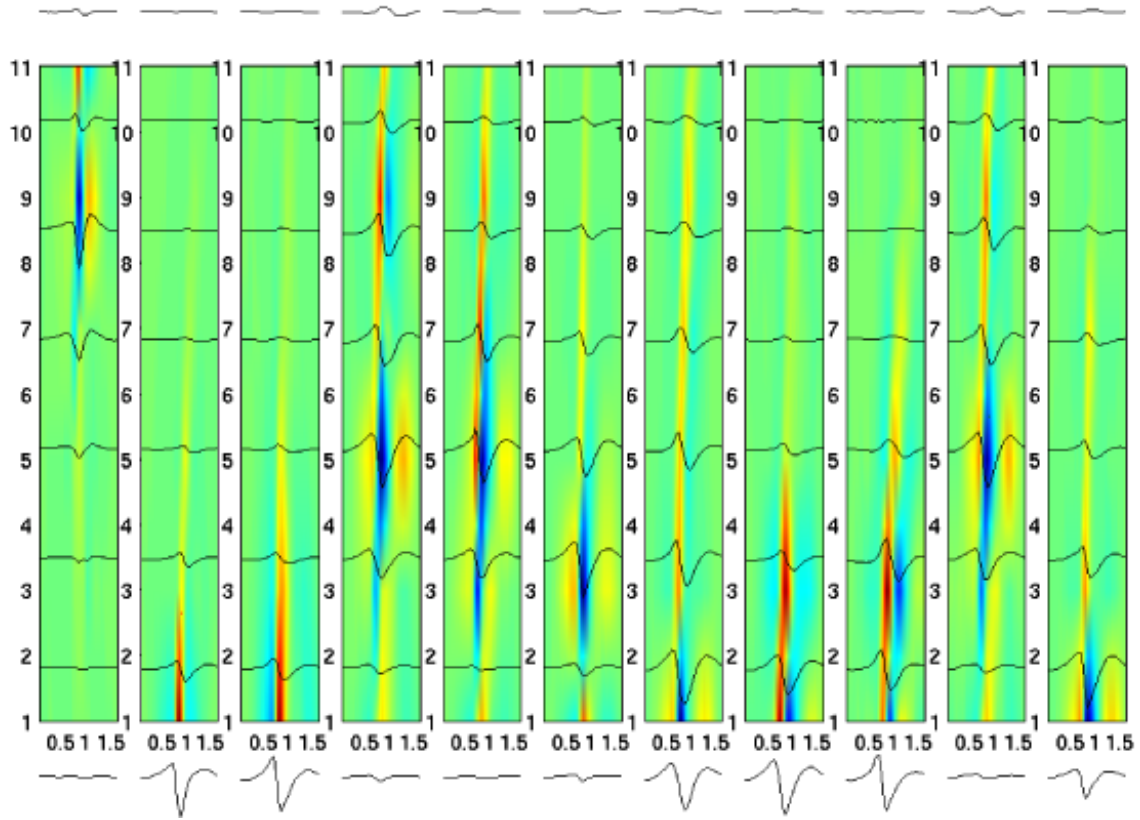


Fig. 12: Current Source Density (CSD) analysis superimposed
on spike waveforms of eleven separately identified single units recorded with a 64 site
probe with on-chip buffering.
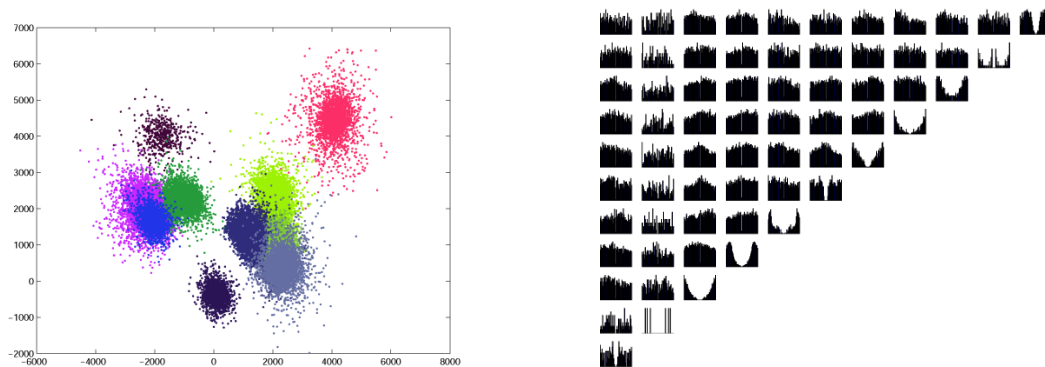
Fig. 13: Cluster diagram (left) showing eleven distinct single units in a 2D projection of optimum feature space. The cross-correlogram at right provides further evidence that these are eleven different single units (see text for explanation.)
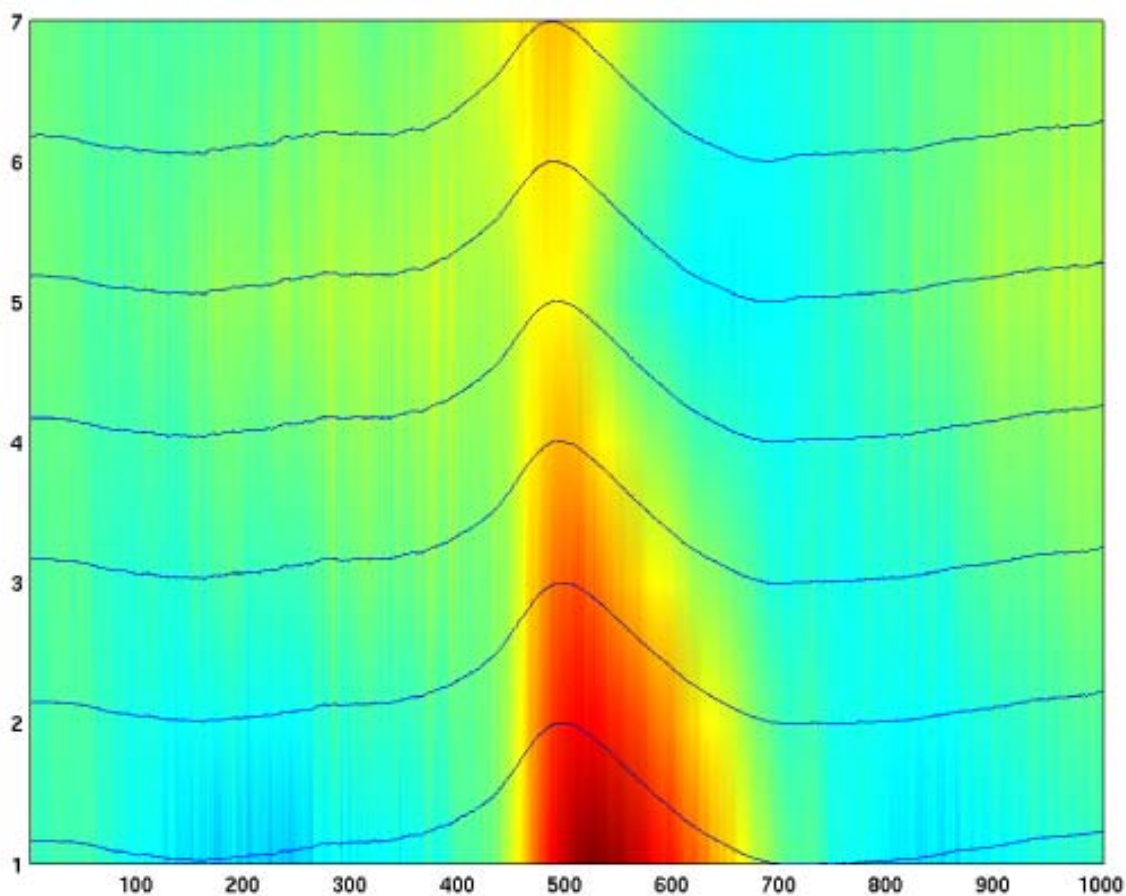


Fig. 14: Current Source Density (CSD) analysis of a delta wave, illustrating a large source in layer 5 and sinks in layer 5 before and after wave onset.

Fig. 12 shows a Current Source Density (CSD) analysis of single unit activity found on various shanks of the 64 site probe.  Each of the eleven panels represents a separately identified single-unit (i.e., cell). The x-axis of each panel is time (in milliseconds) while the color represents the source/sink intensity (red being a source) at each location along the vertical axis (i.e., along a shank) interpolated between each of the eight site locations. The average spike waveform for each of the separated spikes is superimposed on the CSD. The CSD is believed to show evidence of the site of action potential initiation, and of dendritic backpropogation of the action potential. Support for the hypothesis that the eleven separated spikes represent different cells is given in Fig. 13.  In the left panel, a cluster diagram (2D projection of optimal feature space) shows the similarity among, and difference between, features of the waveforms attributed to the same, and different, cells, respectively. The right panel of Fig. 13 shows a cross-correllogram between the spike trains. The presence of a distinct trough on each of the diagonal elements (i.e., zero probability of firing at times close to another firing for these elements) can be attributed to the cell refractory period and indicates that the argument for attributing spikes to different cells is a strong one.  Finally, Fig. 14 shows a Current Source Density analysis and average waveform based on wideband field data obtained during a delta wave. This is an area of great interest to the group, since little is known about the physiological origins of delta waves.

These experiments are the first of their kind: high-density high-channel-count recordings of single units.  The data is currently being analyzed at Rutgers, and expectations are high that there is useful and novel data has already been obtained.  In the meantime, future experiments are being planned which will utilize slightly different probe designs and explore different physiological questions.

## 5. *Development of On-Platform Signal Processing for Chronic Recording Probes*

The 64-site eight-channel active neural recording array (PIA-2) is shown in Fig. 15.  The circuits on this electrode have been tested on the bench top, in-vitro, and in-vivo. A block diagram of the on-probe CMOS circuitry is shown in Fig. 16.  The front-end selector, which is used for electronic positioning of the recording sites, has been tested on the bench top and is fully functional.  Software is currently being developed for the Tucker Davis Technologies (TDT) RP2 data acquisition system to provide the clocking and address data needed to operate the front-end selector in-vivo.  The time-division multiplexer has also been tested on the bench top and is fully functional.  The time-division multiplexer is realized using a two-bit counter and an eight-to-one multiplexer. The measured output of the counter control logic, clock divided by four, is shown in Fig. 17.  During the past quarter, software development has been pursued for demultiplexing the output of PIA-2 and time-division multiplexed in-vivo neural recordings should be obtained in the upcoming quarter.
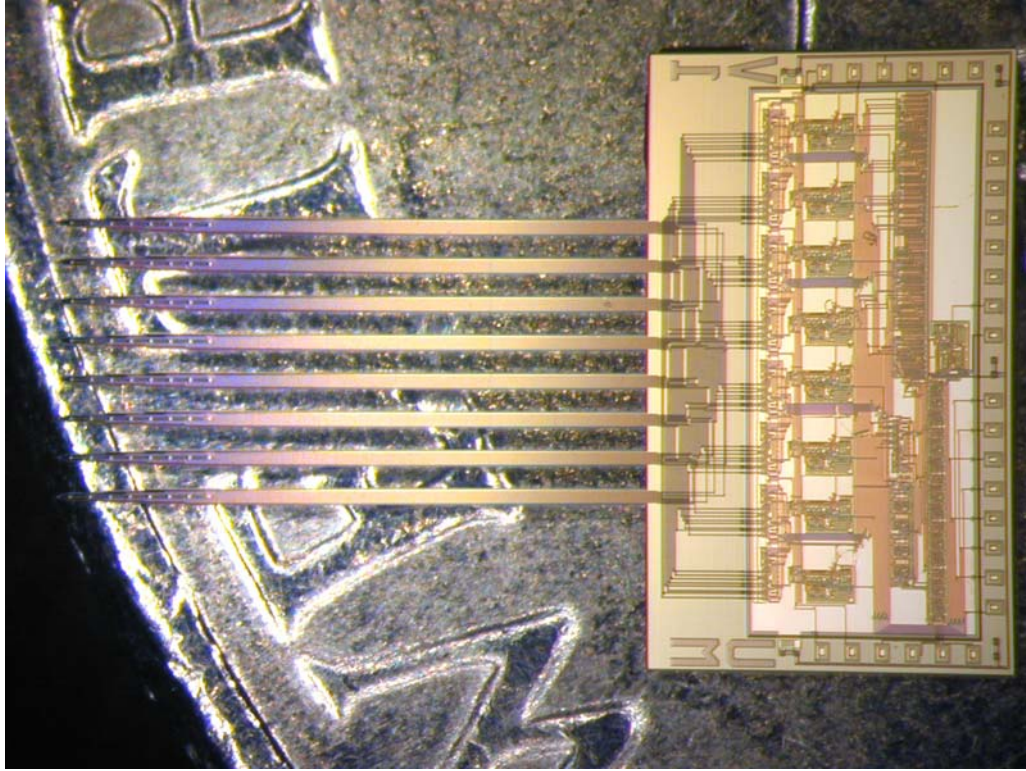
Fig. 15:  PIA-2: A 64-site eight-channel, active neural recording probe

The amplifier configurations included on the different versions of PIA-2 have been tested and characterized.  The feedback configuration used on both versions one and two is shown in Fig. 18.  The p-well where the sub-threshold NMOS transistors are formed is grounded in version one and is tied to the sources of the sub-threshold transistors in version two, Fig. 19.  The response of the amplifier, version 1, verses
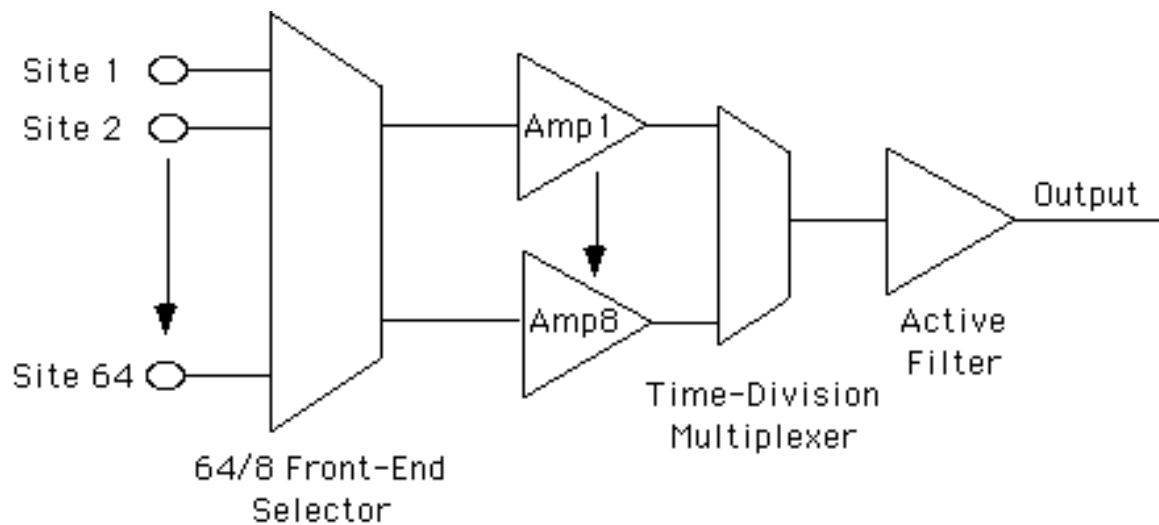


Fig. 16:  Block diagram of the on-chip circuitry on PIA-2.

19

frequency is shown in Fig. 20. The gain of this amplifier is 39.5dB with an upper cut-off frequency of 42kHz. While this amplifier is functional, it is optically sensitive which makes it difficult to test and to use in acute experiments.
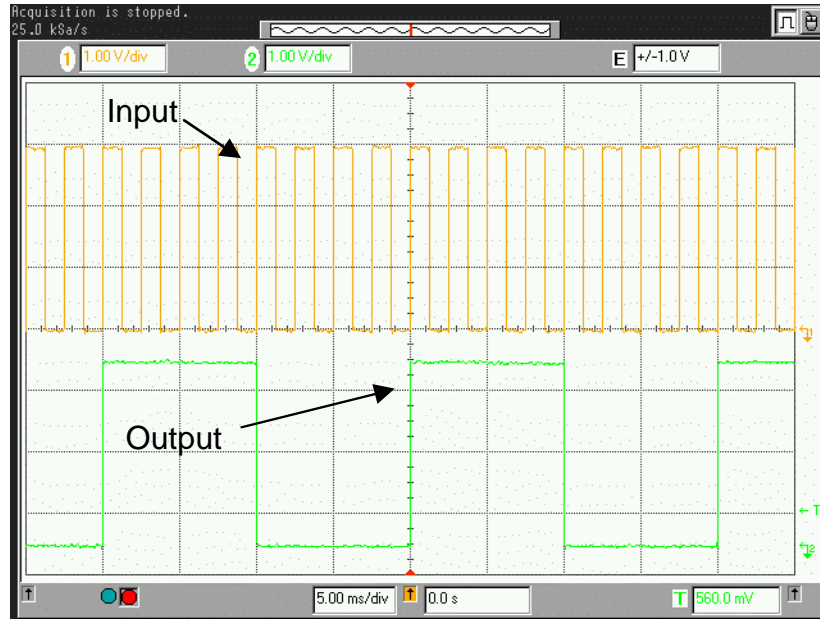


Fig. 17: Measured output of the time-division multiplexer counter
(clock divided by four)
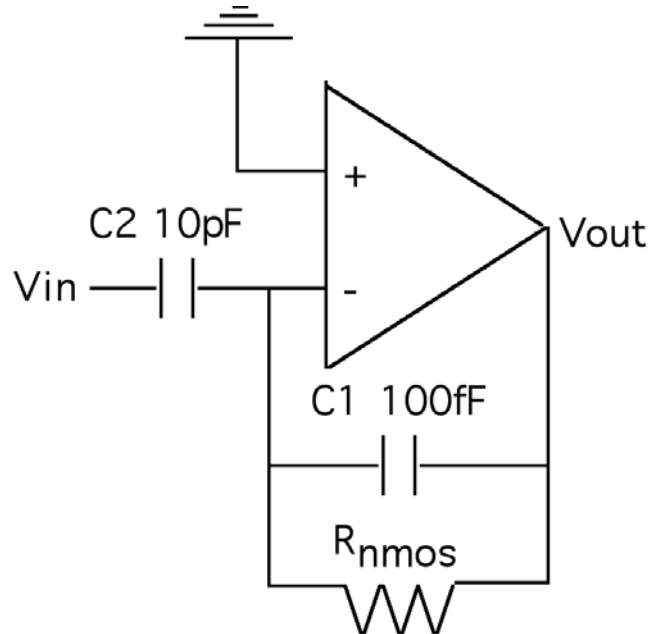

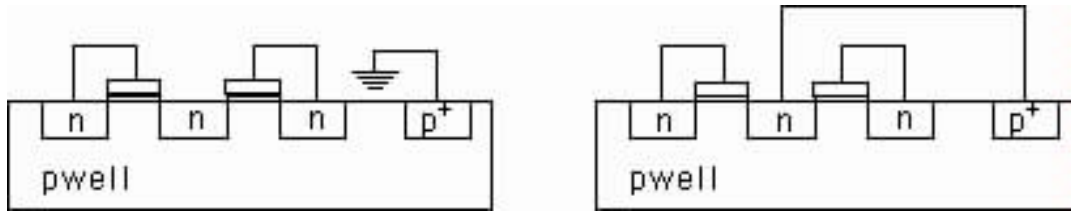
Fig. 18: Sub-threshold NMOS Amplifier Configuration

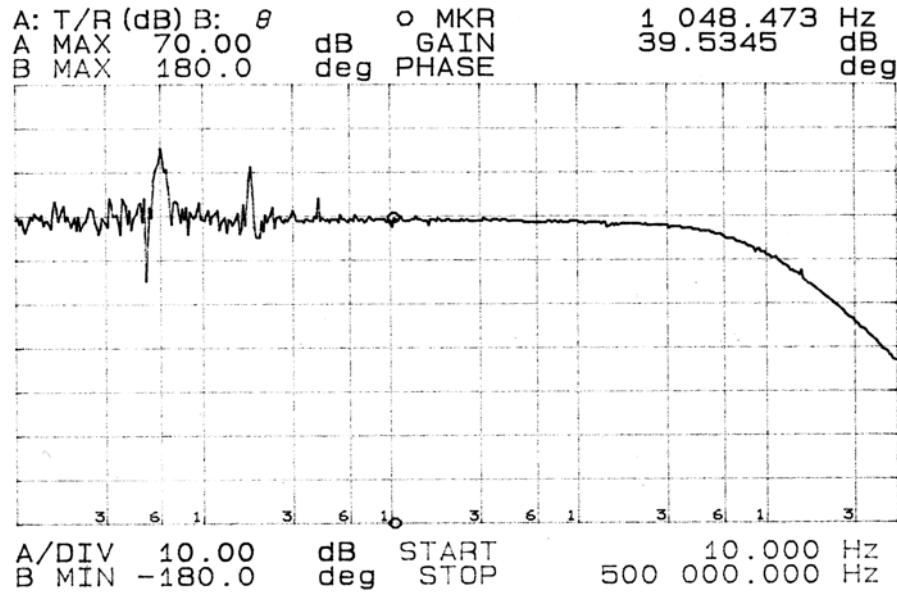Fig. 19: Sub-threshold NMOS transistor implementation: Grounded p-well (left) and p-well tied to source (right).



```
A: T/R (dB) B:  θ           ○ MKR        1 048.473 Hz
A MAX    70.00    dB    GAIN        39.5345      dB
B MAX   180.0    deg  PHASE                      deg
```

```
A/DIV    10.00    dB    START              10.000 Hz
B MIN  -180.0    deg   STOP        500 000.000 Hz
```

Fig. 20: Response of the amplifier with grounded p-well vs. frequency

The version two amplifier, with the p-well tied to the sources of the subthreshold biased transistors, has been tested. These amplifiers were tested at the system level by placing a test signal on one of the sites and monitoring the output of the active filter shown in Fig. 16. The gain of a single channel vs. frequency is shown in Fig. 21. The on-probe electronic system has an in-band gain of 56.6dB and an upper cuttoff frequency of 42kHz. The lower cuttoff frquency of the on-chip amplifier is less than 10Hz, which is below the operating range of the measurment equipment. To test the dc rejection of the on-chip electronics, a 1kHz 2mV sinusiod was placed on a site, first with +500mV of dc offset, and then with a -500mV dc offset. Fig. 22 shows the system response to the signal with +500mV of dc offset, while Fig. 23 shows the system response to input sinusiod with a -500mV dc offset. As can be seen in Figs. 22 and 23, varying the input offset voltage by 1V does not saturate the in-band gain of the amplifier. In addition, the version two amplifier is optically insensitive with all measurments taken in ambient light.
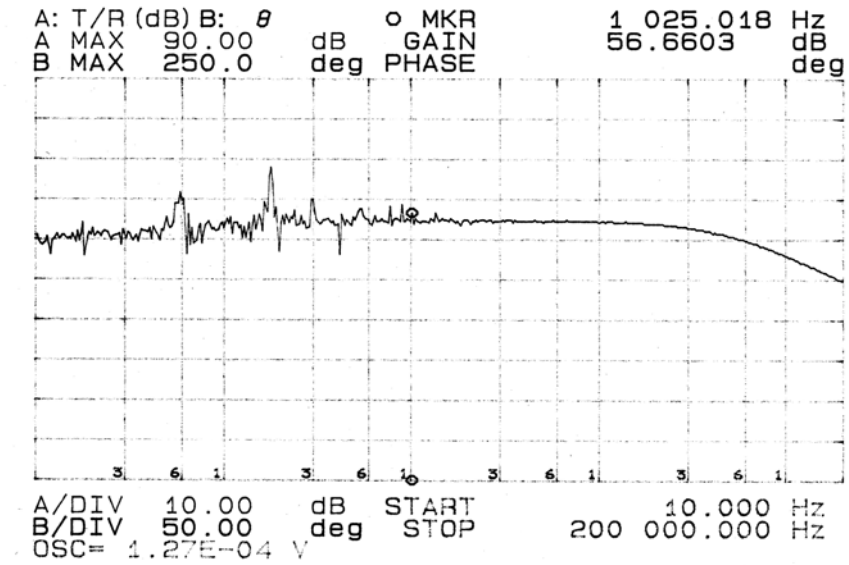
Fig. 21: Gain of the PIA-2 amplifier, version 2, versus frequency.
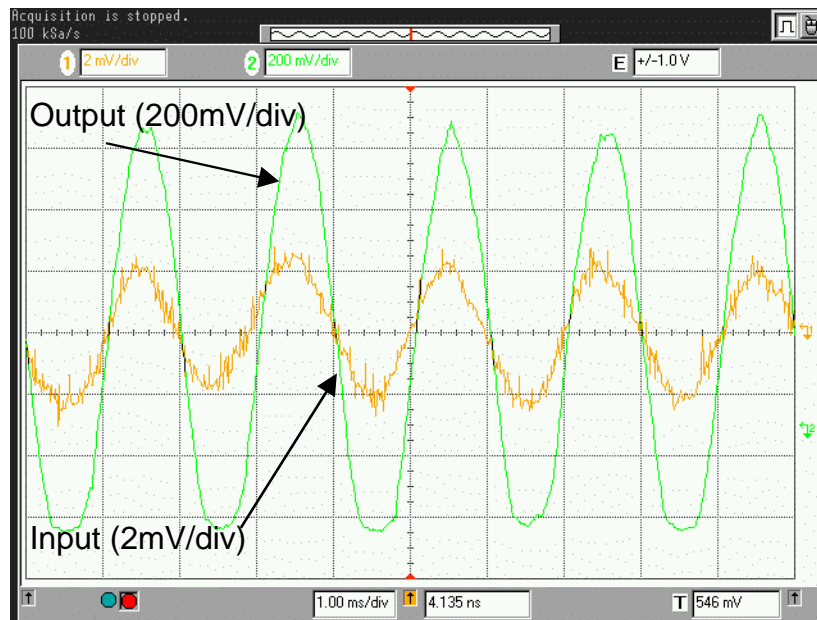


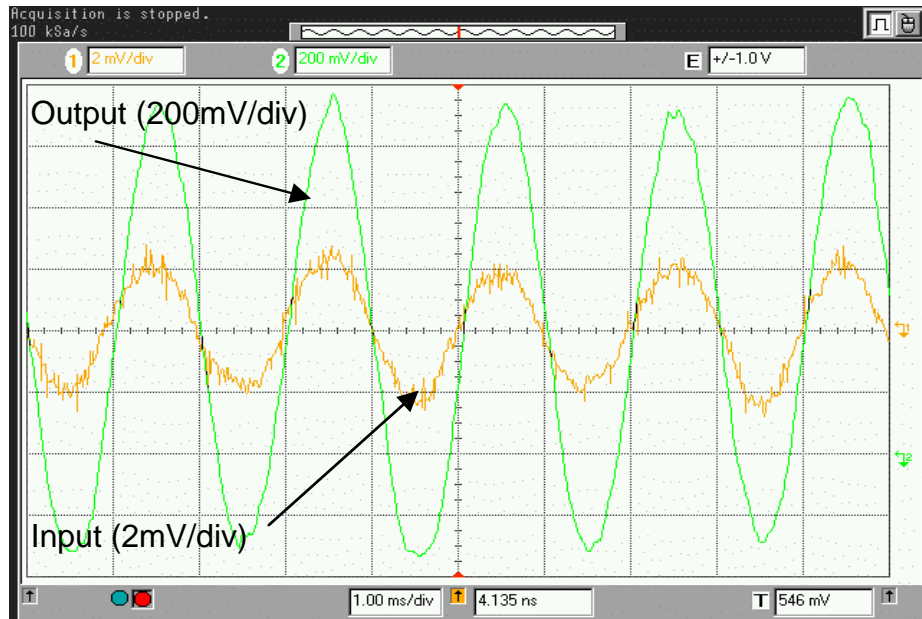Fig. 22: System response to a 2mV, 1kHz, sine wave with a 0.5V DC offset

Fig. 23: System response to a 2mV 1kHz sine wave with a -0.5V DC offset

To test the performance of the on-chip amplifiers in-vivo, the PIA-2, version two electrodes were implanted in the dorsal cochlear nucleus of the guinea pig. Both spontaneous activity, Fig. 24, and activity driven by white burst noise, Figs. 25 and 26, were recorded. The recordings were not time-division multiplexed and the outputs were taken from seven of the eight pre-amplifiers shown in Fig. 16. (Note: one of the pins in the connector was broken, eliminating the possibility of recording from channel eight). Single unit activity was recorded for a period of over two hours and the experiment was terminated without failure of the on-chip electronics. The Tucker Davis Technologies (TDT) RP2 data acquisition system was used to convert the data into digital format and to store the data. Because the RP2 only has two analog input channels, only two sites could be recorded from at any given time despite the fact that activity was present on six of the seven available channels.
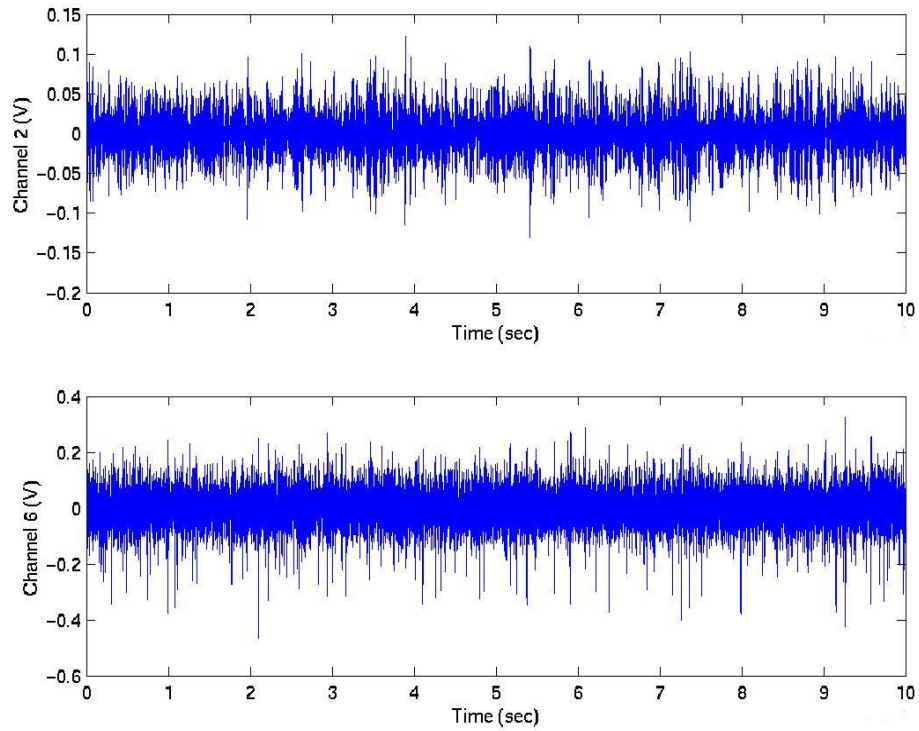
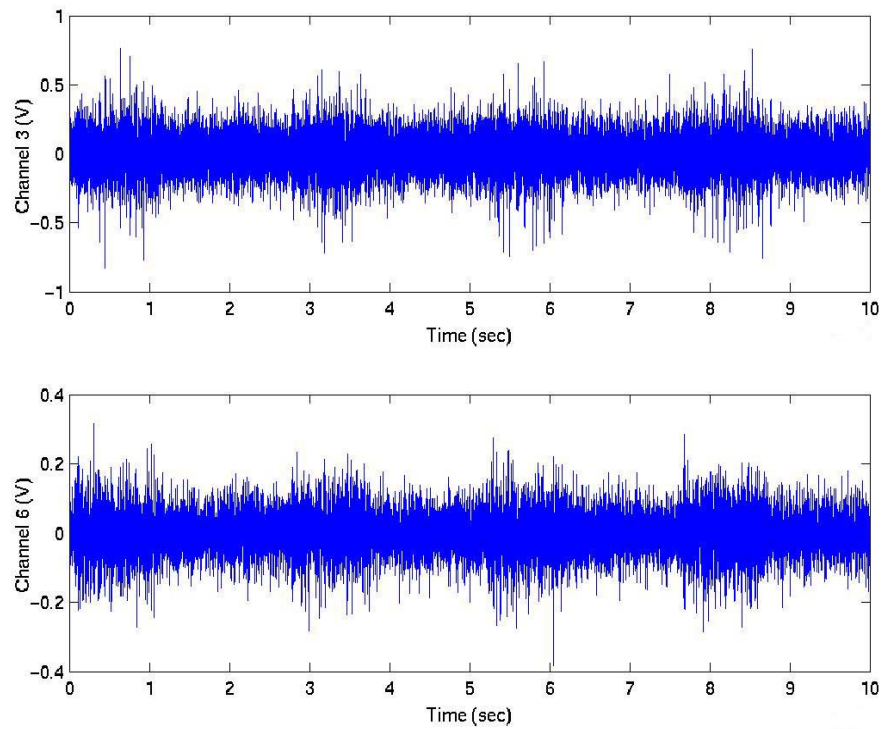Fig. 24: Spontaneous unit activity recorded in the dorsal cochlear nucleus of the guinea pig.



Fig. 25: Unit activity driven by white burst noise recorded in the dorsal cochlear nucleus of the guinea pig
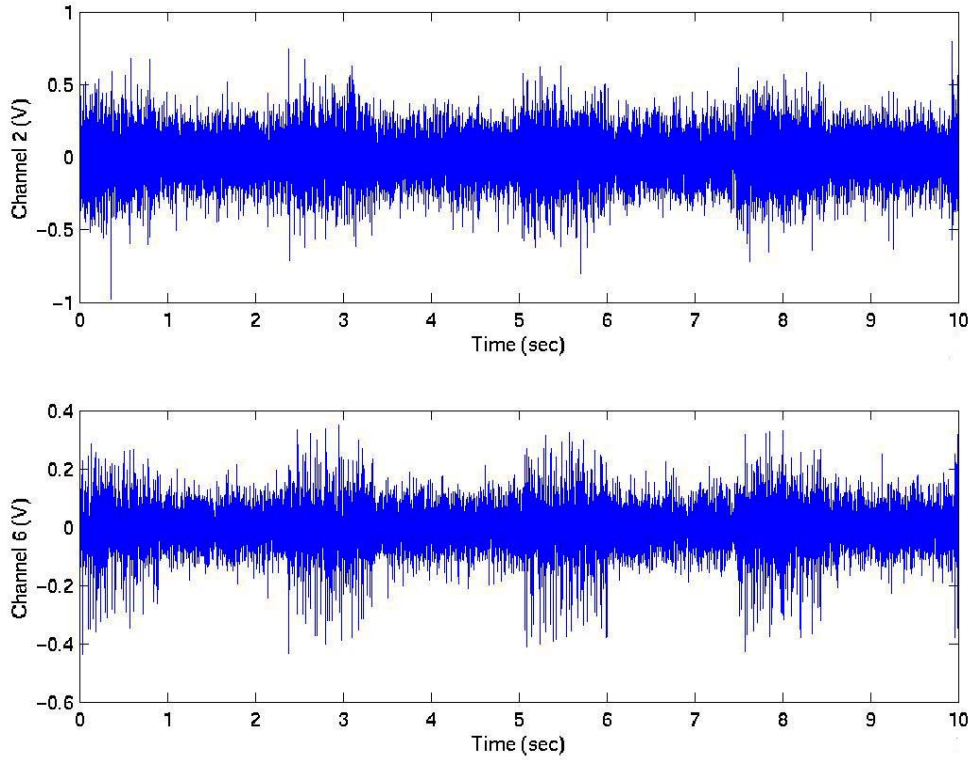
Fig. 26: Unit activity driven by white burst noise recorded in the dorsal cochlear nucleus of the guinea pig

A track and latch comparator, Fig. 27, has been designed to serve as part of a 5-bit successive approximation analog to digital converter. The converter will be used to quantize neural data in-vivo as part of the spike detection unit currently under development. The comparator design features an input pre-amplification stage followed by a latch stage. The pre-amplifier has a low gain to ensure high-speed operation and buffers kickback effects, which can cause glitches on the input signal especially when its impedance is not matched with the reference voltage *Vref*. During the track phase, *Reset* is low and the outputs of inverters one and two are shorted together to prevent hysteresis. Inverters one and two are implemented with an enable, *Reset*, to reduce the static power consumption of the comparator from over 300μW to 37.6μW, Fig. 28. During the latch phase (*Latch* is just *Reset* delayed through four inverters), positive feedback is applied to inverters one and two. This allows very small differential voltages at the output of the pre-amplifier to be driven to near full-scale digital logic levels in a short amount of time. Inverter three is included to obtain a full-scale digital output voltage, which is not possible at the outputs of inverters one and two because the preamplifier loads the outputs of these inverters during the latch phase. A spice simulation of the comparator is shown in Fig. 29.
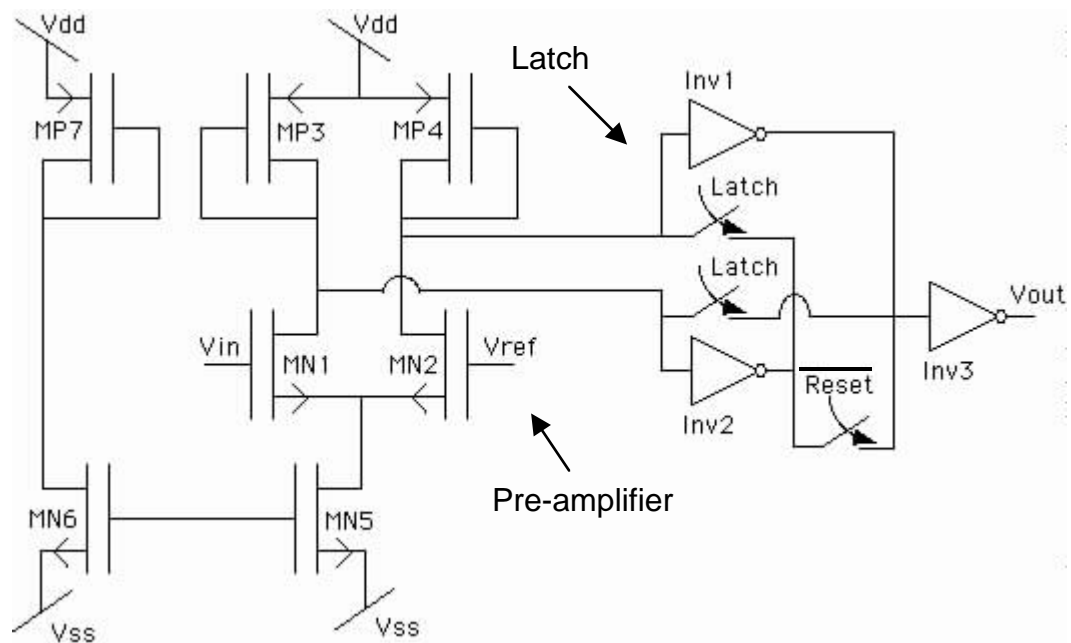
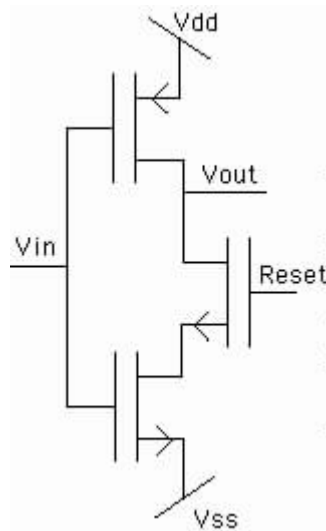Fig. 27: Track and latch comparator schematic



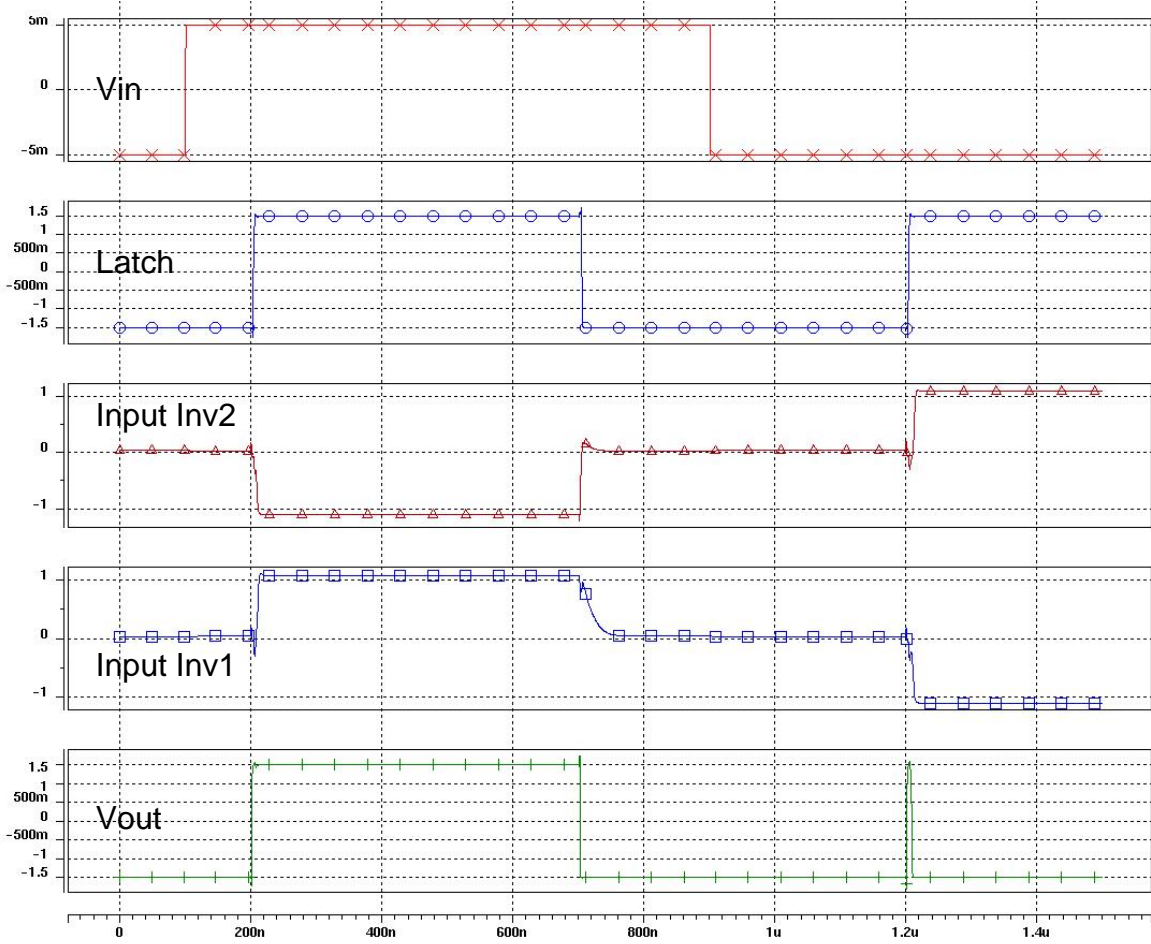Fig. 28: Inverter with enable signal, *Reset*

Fig. 29: Simulated response of the comparator

# 6. Design of a Wireless Telemetry Platform for Multichannel Microprobes

We described the general design of an on-chip transmitter for active multichannel microprobes in last quarterly report. During this past quarter, we have designed in detail both an external transmitter for energy delivery and an implantable on-chip transmitter for digitized data transmission. The external transmitter was built and satisfactory measurement results were obtained.

## 6.1 External Transmitter

The major function of the external transmitter is to deliver energy to the implant, although it also transmits command data for controlling its operation. The design procedures are discussed and measurement results are presented in following sections.

*1) Oscillator*

A crystal Colpitts oscillator was designed to provide carriers for energy and command transmission. Because of the extremely high quality factor of the quartz crystal, an oscillator presents very stable frequency and excellent phase noise performance. The circuit is shown in Fig. 30.
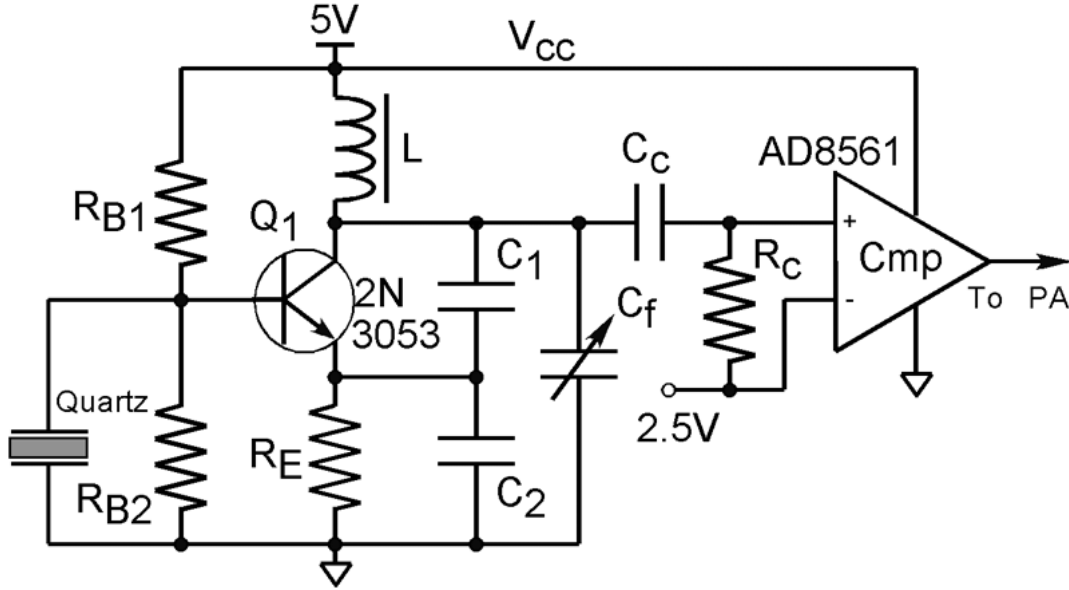


Fig. 30: Crystal oscillator schematic

The crystal works in the series resonance mode to short the transistor's base to ground at the oscillation frequency. $C_1$ and $C_2$ provide positive feedback to the transistor's EB junction. The feedback coefficient is

$$n = \frac{C_1 + C_2}{C_1}$$

As long as initial loop gain

$$A_l = g_m \cdot ((n^2 / g_m) // r_o) > 1$$

the oscillation can start, where $r_o$ is the output impedance of $Q_1$. The AD8561 is a fast comparator used to generate a square wave to drive a class-E Power Amplifier. The nominal oscillation frequency is set at 4MHz and then a 4MHz quartz crystal, L=0.93μH, $C_1$=2nF, $C_2$=10nF, $C_f$=100pF, $R_E$=249Ω, $R_{B1}$=40kΩ, and $R_{B2}$=10kΩ are chosen. The oscillation waveform at the transistor collector and output of the AD8561 were measured as shown in Fig. 31. The power consumption was measured to be 8.3mW. When the 4MHz crystal was replaced by a 20MHz crystal and the feedback ratio was adjusted, 20MHz sinusoid and square waves were observed. The circuit parameters are as following: $C_1$=68pF, $C_2$=330pF, $C_f$=55pF, L=0.5μH, 20MHz crystal. A 1kΩ pull-up resistor was used at the output of the AD8561. A frequency of 20MHz may be used later to achieve a higher command bit rate.
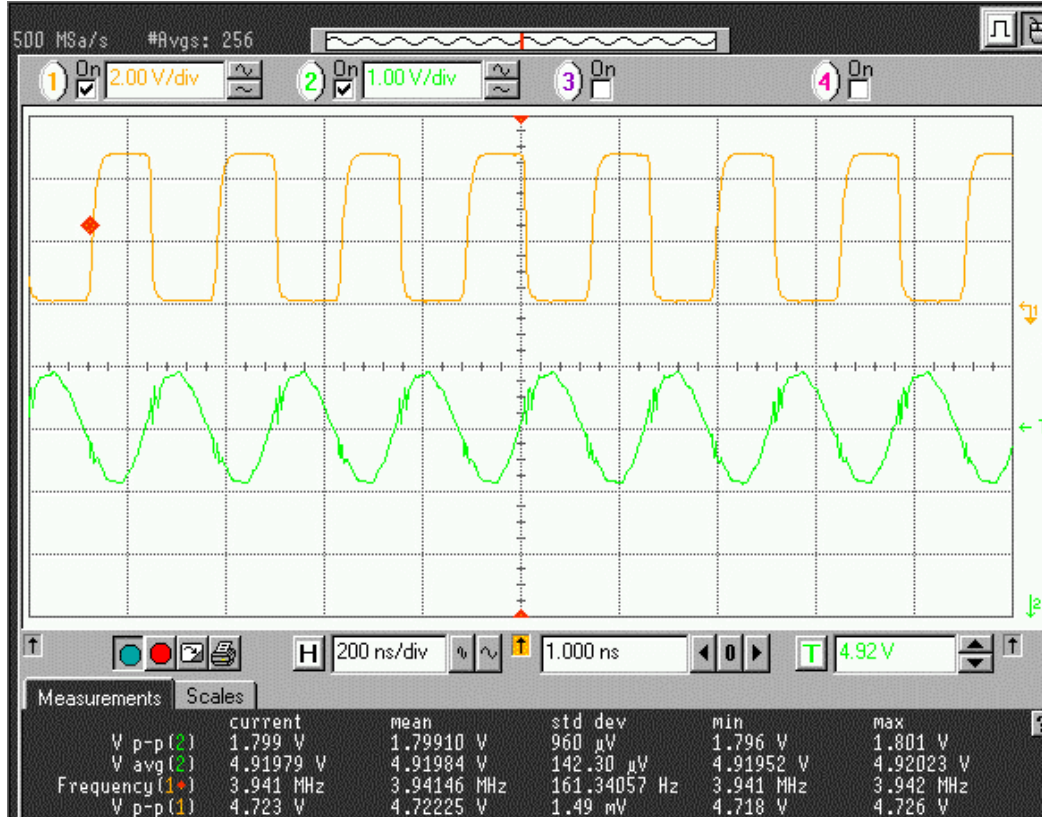
Fig. 31. The waveform of the oscillator and comparator output

*2) Class-E Power Amplifier*

A class-E power amplifier was chosen for use in the external transmitter because of its inherent high efficiency as discussed below:
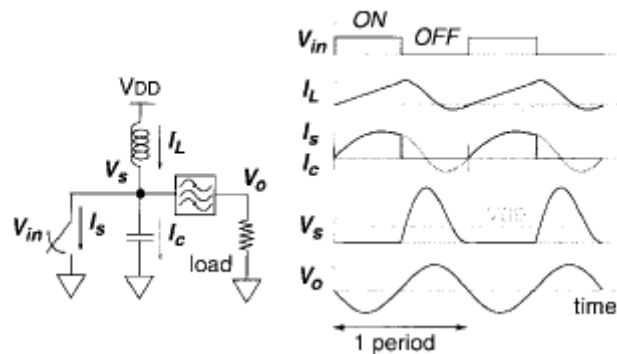


Fig. 32:  A simplified class-E power amplifier and its steady-state operation[1]

---

[1]  K. Tsai, P. Gray, "A 1.9-GHz, 1-W CMOS Class-E Power Amplifier for Wireless Communications", *IEEE JOURNAL OF SOLID-STATE CIRCUITS, VOL. 34, NO. 7,* July 1999.

Fig. 32 shows a typical schematic for a class-E power amplifier. The input signal $V_{in}$ turns on and off the switch, which is usually implemented with a power BJT or MOS transistor. The inductor acts as an RF choke to maintain a nearly constant current. When the switch is on, the current can go through the switch to ground; when the switch is off, the current is driven to the load and charges the parallel capacitor. The tuned bandpass filter passes the fundamental component of Vs to the load, creating a sinusoidal output. At optimum steady-state operation, Vs returns to zero when the switch is turned on, and Is returns to zero when the switch is turned off. Consequently, the power consumed by the switch is zero under ideal operation so that all power is delivered to load, i.e., the theoretical efficiency of a Class-E power amplifier can reach 100%.

We designed a class-E power amplifier as illustrated in Fig. 33(a). $C_c$ and $R_c$ form a high pass filter, which sets the gate DC potential at ground so that the AC component (square wave) from the oscillator turns the power MOSFET TN0620 on and off. $C_2$, $L_t$ form a bandpass filter, $R_L$ is the load, and $R_t$ is the parasitic resistance of $L_t$. $C_1$ and $C_2$ can be tuned so that the Class-E power amplifier works in an optimum configuration. The design formulas are given as[2]

$$Q = \frac{\omega \cdot L_t}{R}$$

where $\omega$ is the operating frequency and R is total resistance, including $R_t$ and $R_L$.
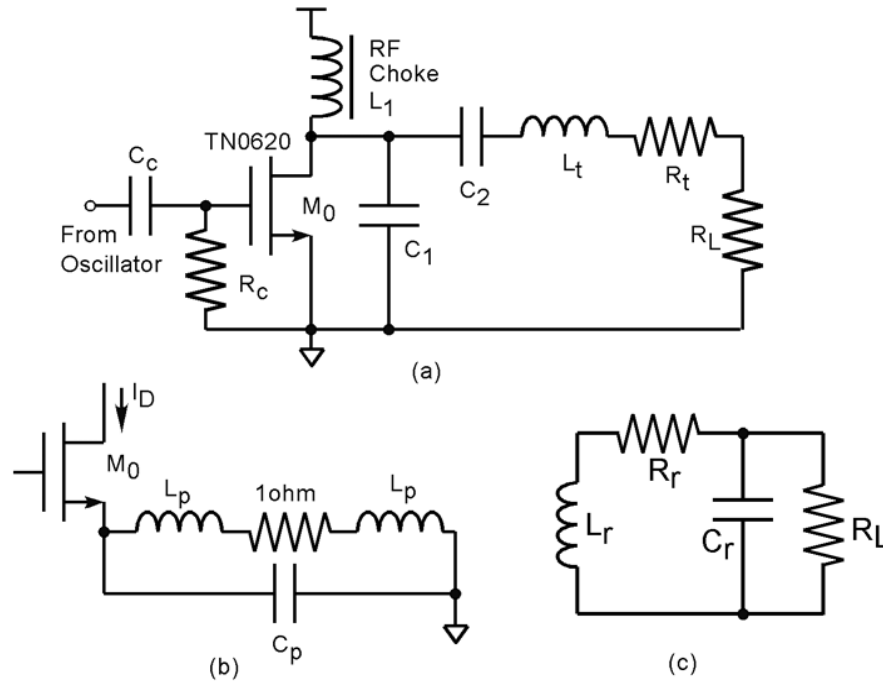


Fig. 33: a) Implementation of a Class-E power amplifier; b) measurement configuration for $I_D$ (c) power receiving circuitry

[2] N. O. Sokal, A.D. Sokal, "Class-E, A New Class of High-Efficiency Tuned Single-Ended Power Amplifiers", *IEEE JOURNAL OF SOLID-STATE CIRCUITS, VOL. SC-10, JUNE 1975*

$$C_1 = \frac{1}{\omega R(\pi^4/4+1)(\pi/2)}$$

$$C_2 = C_1(\frac{5.447}{Q})(1+\frac{1.42}{Q-2.08})$$

The transmitter inductor used in Fig. 33(a) was actually a 29-turn coil with diameter of 26mm and length of 31mm, built using AWG24 copper wire (wire diameter $\phi$ = 0.5mm). The inductance can be estimated by using formula given by Terman[3]

$$L_0 = Fn^2 d$$

where n is the number of turns, d (inch) is the diameter of the coil, F depends on the ratio of coil's diameter to coil's length and is tabulated in the literature. The inductance was measured using an HP 4284A, which can measure inductance and Q up to 1MHz. The measured results were close to the calculated ones, as shown in Table 1, where the receiver coil $L_r$, used in Fig. 33(c) is also tabulated for convenience. It will be discussed later.

| Coils | Calculated inductance | Measured inductance |
|---|---|---|
| **Transmitter coil** 29-turn single layer diameter = 26mm length = 31mm, AWG 24 wire $\phi$=0.5mm | 13.3μH | At 1MHz, L=16μH Q=120, R=0.8Ω |
| **Receiver coil** 51 turns multi-layer diameter = 10mm length = 2mm AWG 44, $\phi$=0.05mm | 44.1μH | At 1MHz, L=51μH Q=42, R=7.5Ω |

Table 1: Coils' configuration and inductance

In the first measurement, the nominal operating frequency was set at 1MHz and $V_{DD}$ was 3.0V. The following circuit component values were used: $R_L$=5Ω, Q=17.3, $C_1$=3nF, and $C_2$=1510pF. The measurement results support the foregoing theoretical analysis, as shown in Fig. 34, where channel one was the control signal applied to the gate of the switch transistor; channel two recorded the drain voltage; channel three was the voltage across the load, and channel four recorded the voltage drop across a 1Ω resistor due to the drain current, as illustrated in Fig. 33(b).

At the position of cursor A in Fig. 34, the gate signal turns off the transistor, so the drain current abruptly changed to zero, and the drain voltage began to increase. At the position of cursor B, the control signal turns on the transistor, whereas the drain

[3] F. E. Terman, "Radio Engineers' Handbook", McGraw-Hill Book Company, Inc, 1943

voltage had already fallen to zero and the drain current begins to increase. A measured efficiency of 82% was obtained. The results @1MHz are summarized below.
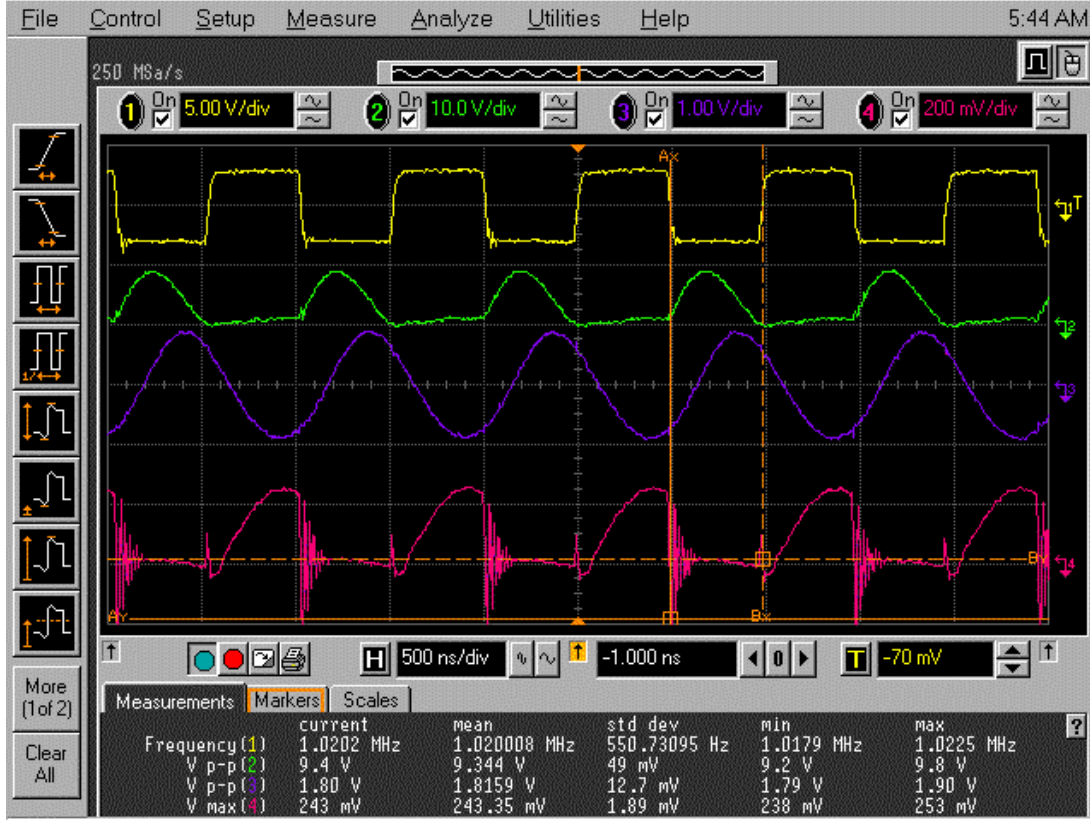


Fig. 34:   Class-E power amplifier operation @ 1MHz

| V$_{DD}$ | Drain Voltage | Drain Current | Load Current | Efficiency |
|---|---|---|---|---|
| 3.0V | 9.34V Max | 243mA max | 360mA (p-p) | 82% |

Ringing was obvious at the falling edge of the drain current due to the transient response of the parasitic resonant circuit, illustrated in Fig. 33(b). The parasitic resonant circuit is composed of the parasitic inductances of resistor leads, L$_p$, and parasitic capacitance of breadboard, C$_p$.  To do a rough evaluation, the total lead inductance was about 20nH (1nH/mm) and the breadboard parasitic capacitance was about 6pF (obtained by measurement) so the calculated ringing frequency is 459MHz, which matches the measured ringing frequency.  The Q$_p$ of this parasitic resonant circuitry can be evaluated as

$$Q_p = \frac{\sqrt{L/C}}{R} = 57.7$$

Therefore, the high Q$_p$ leads to high peaking and a long settling time, which is observed in the measurements.  A class-E power amplifier will be built on a printed board later; a much better transient response can be expected.

The class-E power amplifer was also tuned to work at 3.58MHz and 4MHz; a measured result at 4MHz is shown in Fig. 35. The results @4MHz are summarized below. The waveforms in Fig. 35 are similar to those in Fig. 34. The drain current is not measured due to long transient response in the measurement as illustrated in Fig. 34.

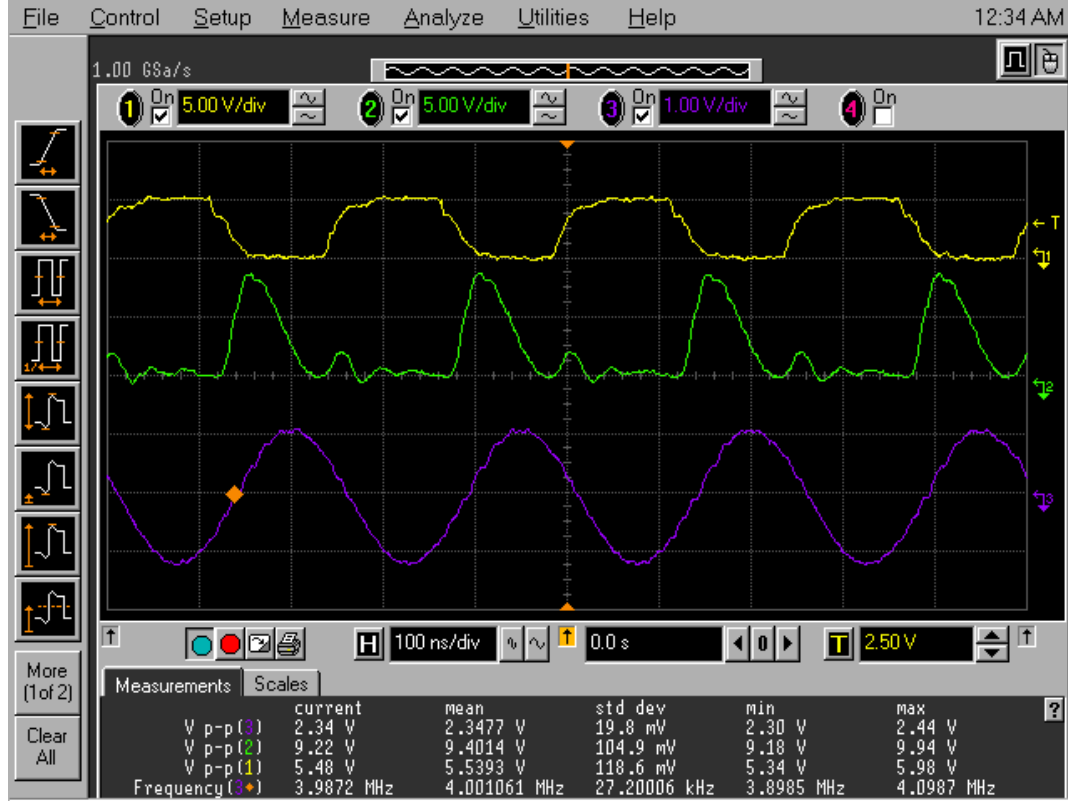| $V_{DD}$ | Drain Voltage | Drain Current | Load Current | Efficiency |
|---|---|---|---|---|
| 3.0V | 9.40V Max | — | 469mA (p-p) | 79% |



Fig. 35: Class-E power amplifier operation @ 4MHz

*Power Receiving Test*

As shown in Fig. 36(a), a power receiver circuit was built to receive power from the transmitter coil by inductive coupling. $C_r$ is tuned so that the receiver circuit resonates at 4MHz. At the resonant frequency the circuit in (a) is equivalent to (b) if Q is high, which is the case for our experiment, and

$$R_{r2} \cong \frac{1}{(\omega C_r)^2 R_L}$$

The receiving coil structure, inductance, quality factor were listed in Table 1. i.e., $L_r$=51μH, $R_r \cong 7.5\Omega$ @1MHz. The parameters are listed below. We assume that the parameters at 4MHz do not differ much from those at 1MHz.
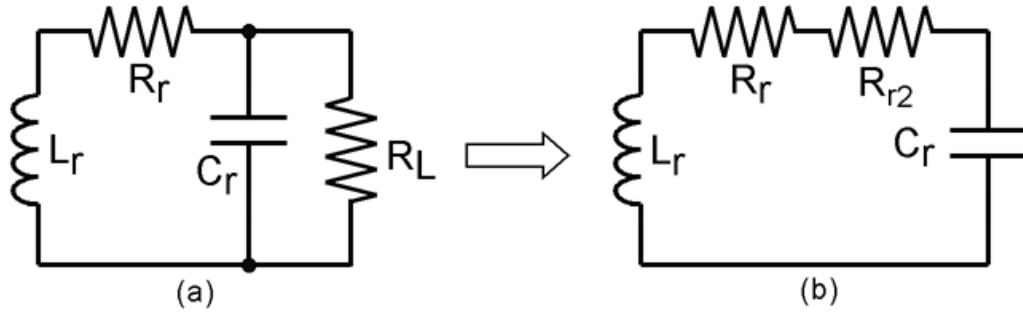
Fig. 36: Power receiving circuitry

| $L_r$ | $R_r$ | $C_r$ | $R_L$ | $R_{r2}$ |
|-------|-------|-------|-------|----------|
| 51μH | 7.5Ω | 33pF | 487Ω | 3.0kΩ |

We still used the transmitter circuit shown in Fig. 33 (a), operating at 4MHz. But $R_L$ was set to zero this time to induce higher current in the transmitter coil, and $V_{DD}$ was set to 9.0V. When the receiver coil was separated by 10mm from the transmitter coil, the measurement results are shown in Fig. 37, where channel 3 was the voltage across the transmitter coil and channel 4 was the voltage across the receiver's load resistor. The voltage across the primary coil was about 300V. The induced EMF across $R_L$ was 3.34V (rms), so the received power was 22.9mW. Because the power consumption of the transmitter was 2.1W, the overall efficiency of the power delivery system (10mm separation) was 1.09%.

| Voltage on $L_t$ | Voltage on $L_r$ | *Received Power* | Total consumed power | Overall efficiency |
|------------------|------------------|------------------|----------------------|--------------------|
| 293V p-p | 9.7V p-p | 22.9mW | 2.1W | 1.09% |

The tuning capacitance also affected the received power. When the capacitance changed from 33pF to 43pF, the induced EMF voltage decreased by 6%. The load impedance degraded the Q of the receiver circuit greatly. It was noticed that the measured unloaded $Q_r$ of the receiver coil was 42 at 1MHz. Since parasitic resistance of the coil didn't change much from 1MHz to 4MHz, the unloaded $Q_r$ was calculated to be 168, whereas the loaded $Q_r$ became 0.43 at 4MHz when driving a 487Ω resistor.

*Demonstration of Wireless Power Transfer*

The wireless system was set up in prototype form to demonstrate its operation for power transfer. The distance between the transmitter coil and receiver coil was 8mm. The power supply of the Class-E power amplifier in the transmitter was increased slowly to provide more power to the receiving circuit. When the power supply reached 5.6V, the chip began to function well. If the power supply continued to increase, induced EMF

voltage across the coil kept increasing with the received power, but the on-chip regulator outputs stayed constant. The waveforms of concern are shown in Fig. 38(a).
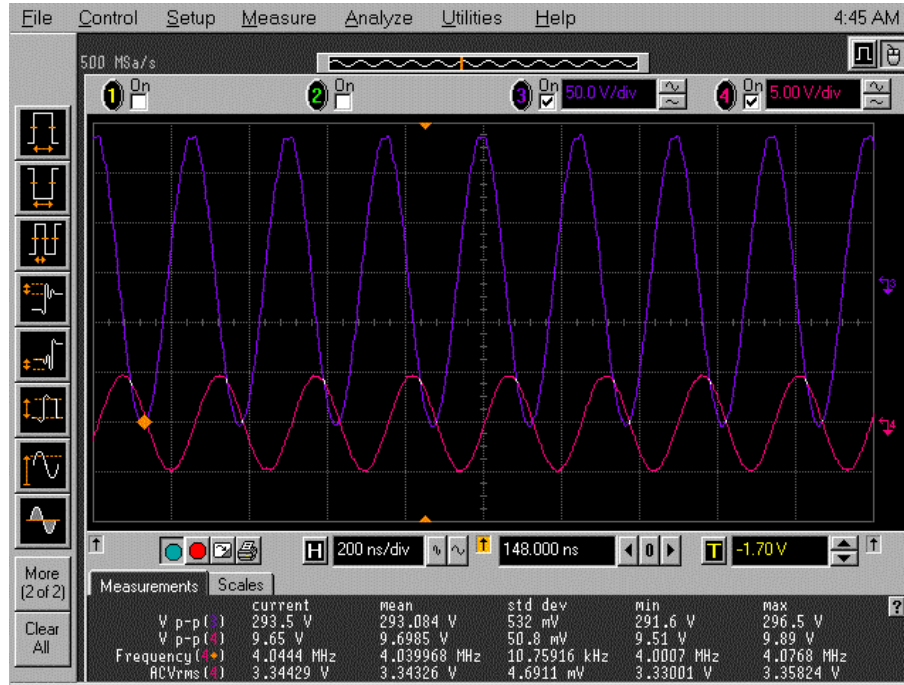


Fig. 37: Voltages across transmitter coil and receiver's load (10mm separation)
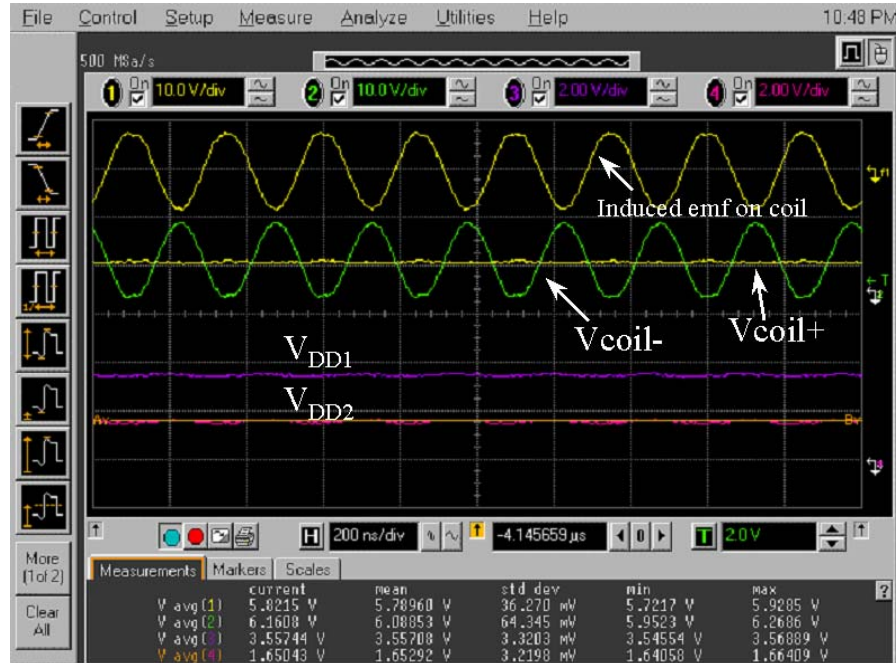


Fig. 38: (a) Measurement results for the wireless powered chip

The results are summarized below.

| Channel | Signal | Average | Peak-Peak |
|---------|--------|---------|-----------|
| 1 | VCoil+ | 5.79V | 1V |
| 2 | VCoil- | 6.09V | 13.4 |
| Function 1 | Coil+ - Coil- | — | 15.5V |
| 3 | $V_{DD1}$ | 3.55V | 121mV |
| 4 | $V_{DD2}$ | 1.65V | 76mV |

To further test the remote power transmission, the on-chip ASK demodulator was tested. The results are shown in Fig. 38(b), where channel one was the voltage on the external transmitter's load, showing the modulation depth, channel two was a 60kHz modulation signal, channel three was the output of the on-chip demodulator, and channel four was the regulator output.
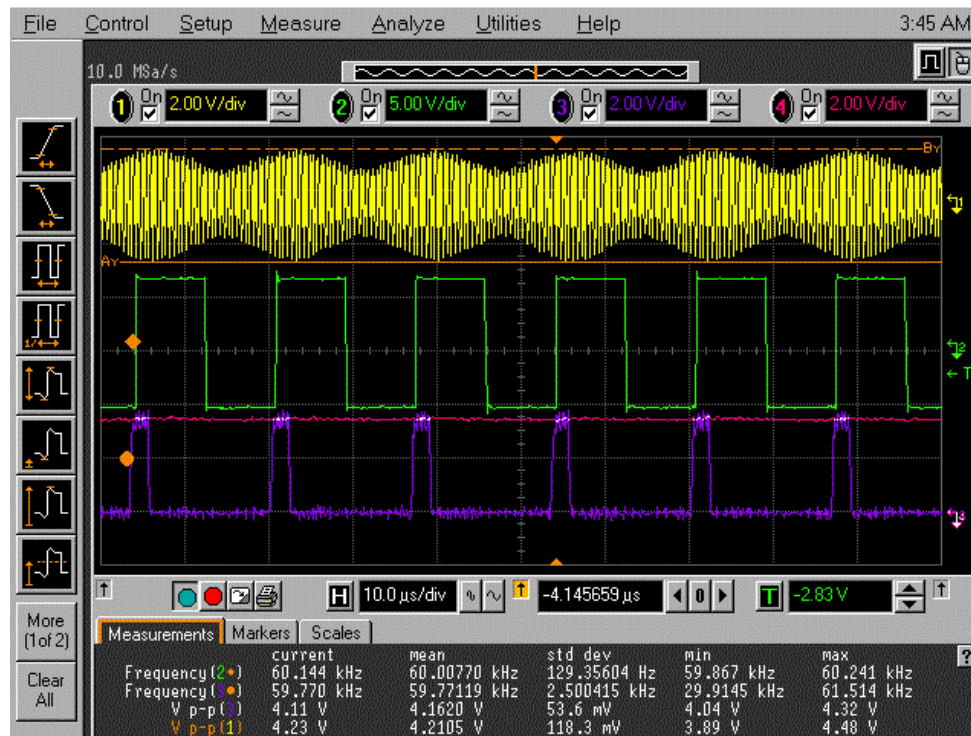


Fig. 38(b):  Testing the ASK demodulator

For this measurement, the carrier frequency was 4MHz, the data rate was 60kbps, and the modulation depth was 30%. The regulator output remained constant at 3.5V.  The ASK demodulator correctly recovered the data from the amplitude-modulated carrier. The ASK demodulator was also tested at other data rates; results are summarized below:

| Date rate | Carrier frequency | Required Modulation depth |
|-----------|-------------------|---------------------------|
| 60kbps | 4MHz | 30% |
| 30kbps | 4MHz | 20% |
| ≤20kHz | 4MHz | <15% |

In conclusion, wireless powering of the implant chip was demonstrated and has yielded satisfactory results.

*(3) Transmitter energy limits*

The IEEE recommends a standard for safety with respect to RF exposure. Because wireless powering of implanted devices is a situation where the patient is aware of the exposure, it is regarded as *"Controlled Environment"*. The maximum permissible exposure (MPE)[*] for Controlled Environments is tabulated in Table 2.

*Electromagnetic Fields*

| *Frequency (MHz)* | *Electrical Field (V/m)* | *Magnetic Field (A/m)* | *Power density(S) E-Field, H,Field ($mW/cm^2$)* | *Averaging Time $\|E\|2, \|h\|2$, or S (minutes)* |
|---|---|---|---|---|
| 0.1-3.0 | 614 | 16.3/f | 100, $10,000/f^2$ | 6 |
| 3.0-30 | 1842/f | 16.3/f | $900/f^2$, $10,000/f^2$ | 6 |
| 30-100 | 61.4 | 16.3/f | 1.0, $10,000/f^2$ | 6 |

f=frequency in MHz

Table 2: MPE for controlled Environment[4]

* Only frequency ranges of concern in our application are listed

We can note the different limits for electrical field and magnetic field, because they have different biological effect on human body. Usually the magnetic field limits are much more relaxed than the electrical field limits. Since only a small part of the body is exposed to the RF magnetic field in our case, relaxation of the power limit can be applied, as listed in Table 3.

| | *Frequency in GHz** | *Peak Value of Mean Squared Field* | *Equivalent Power density(S) ($mW/cm^2$)* |
|---|---|---|---|
| Controlled Environment | 0.0001<f<0.3 | <20 $E^2$ or $20H^2$ ** | N/A |

Table 3: Relaxations for Partial Body Exposures[4]

* Only frequency ranges of concern in our application are listed

** E and H are the spatially averaged values from Table 2

The relationship between the H-field/E-field and power density in vacuum or air is as follows:

$$S = E^2/Z_0 = H^2 \cdot Z_0$$

where $Z_0$ is intrinsic space impedance, and

$$Z_0 = \sqrt{\frac{\mu_0}{\varepsilon_0}} = 376.8 ohm$$

---

[4] IEEE Standards Coordinating Committees, "IEEE Standard for Safety Levels with Respect to Human Exposure to Radio Frequency Electromagnetic Fields, 3kHz to 300GHz", *IEEE C95.1-1991, P13, P20*

Then the H-field and power density limits for frequency of concern are listed below:

| Frequency(MHz) | 1 | 4 | 10 | 20 |
|---|---|---|---|---|
| H-field limit (A/m) | 72.8 | 18.22 | 7.28 | 3.64 |
| Power Density (W/cm$^2$) | 200 | 12.5 | 2 | 0.5 |

Table 4:  Limits in power transmission of the telemetry

If 4MHz is used as carrier frequency and the fabricated transmitter coil (diameter = 26mm) is chosen to power the implant, the power driven to the coil is set to be lower than

$$S(4MHz) \cdot \pi \cdot d^2 / 4 = 66(W)$$

in accordance with the IEEE standard for RF exposure. The total power used in the demonstration was less than 2W, much lower than the limit.

*(4) Coil Design*

An inductively coupled coil system was used to provide power and information to the implant, as illustrated in Fig. 39.  Both primary and secondary circuits are tuned to resonate.
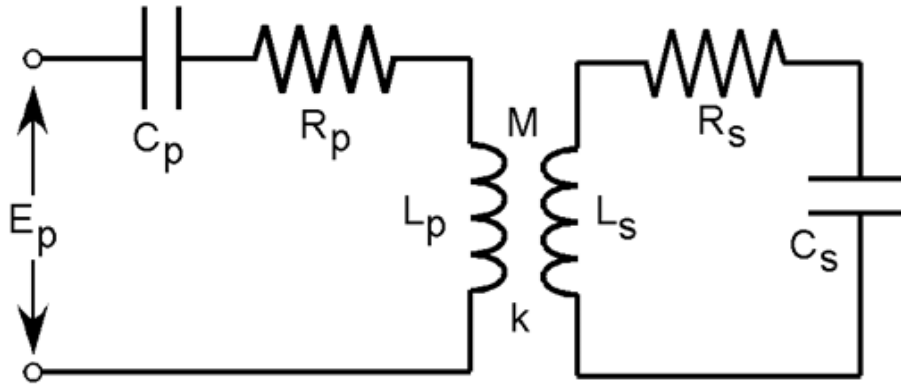


Fig. 39:  The inductive coupling link

It is important to optimize the primary and secondary coils so that the energy transmission system has high efficiency.  Beginning with the secondary coil, it is better to have large cross section and more turns to receive more energy from the magnetic field. By Faraday's law, the induced emf is

$$v = -\frac{d}{dt} \iint_S \vec{B} \cdot \vec{ds}$$

where B is magnetic flux density and S is the surface enclosed by the coil wire. For an n-turn coil, $S_1$ is the area enclosed by one-turn, then

$$S = n \cdot S_1$$

Thus, larger size benefits the energy reception; however, size is limited by the implant. Considering the size acceptable for an implant, a 51-turn receiving coil with diameter of 10mm was built.   It will be used in later analysis. The relationship between magnetic flux density B and magnetic field H is

$$B = \mu_0 \mu_r H$$

Thus, it is beneficial to use ferrite core with high $\mu_r$ if the ferrite core is biocompatible.

The primary coil configuration can be chosen by numerical simulation in MATLAB.  The mutual inductance and self inductances of the coils can be evaluated by using formulas provided by Terman[3]; these formulas are in good agreement with measurement, as shown in Table 1 and verified in T. Akin's thesis[5]. The coupling coefficient k is defined as

$$k = \frac{M}{\sqrt{L_1 * L_2}}$$

It represents the extent of coupling between the primary and secondary coils.  Suppose the distance between the primary and secondary coils is 10mm.  Then the simulation results for k are shown in Fig. 40.
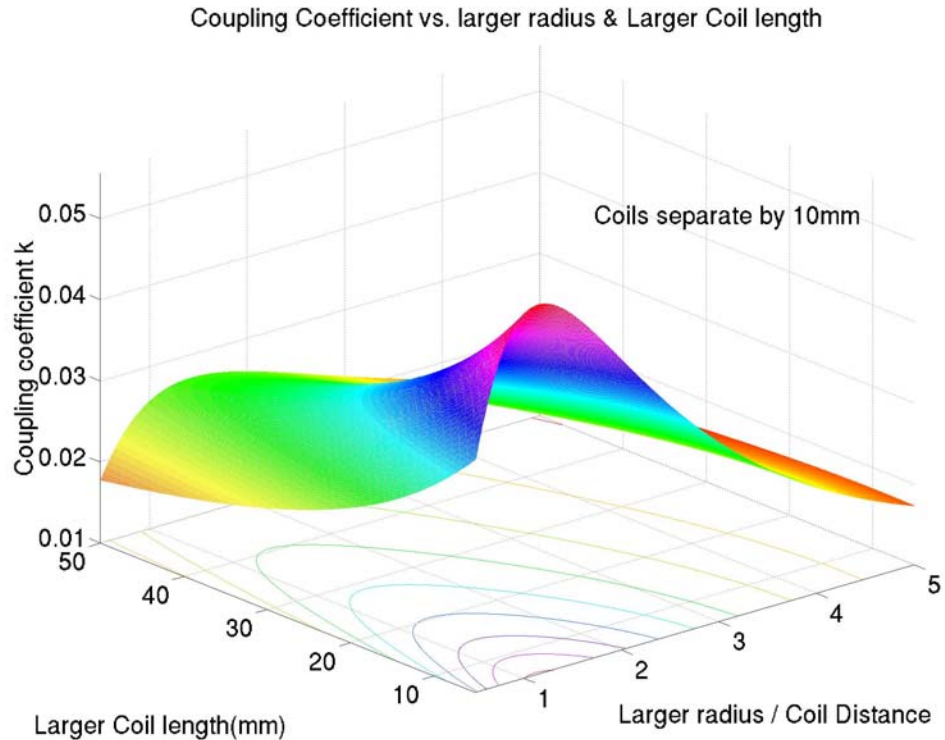


Coupling Coefficient vs. larger radius & Larger Coil length

Fig. 40:  The effect of primary coil configuration on coupling coefficient (separation is 10mm)

[5] T. Akin, Ph.D. Thesis, The University of Michigan, 1994

It is clear that when the coil radius is close to 1~1.5 times the coil separation distance, and the turns of the coil concentrate at the nearest plane to the secondary coil, the coupling coefficient approaches the optimum. This result also agrees with C. Zierhofer's conclusion[6]. Similar simulations were carried out for situations such that the coils were separated by 7mm, 30mm and 50mm; the results are the same. Only the simulation for a 7mm separation is shown in Fig. 41 to save the space.
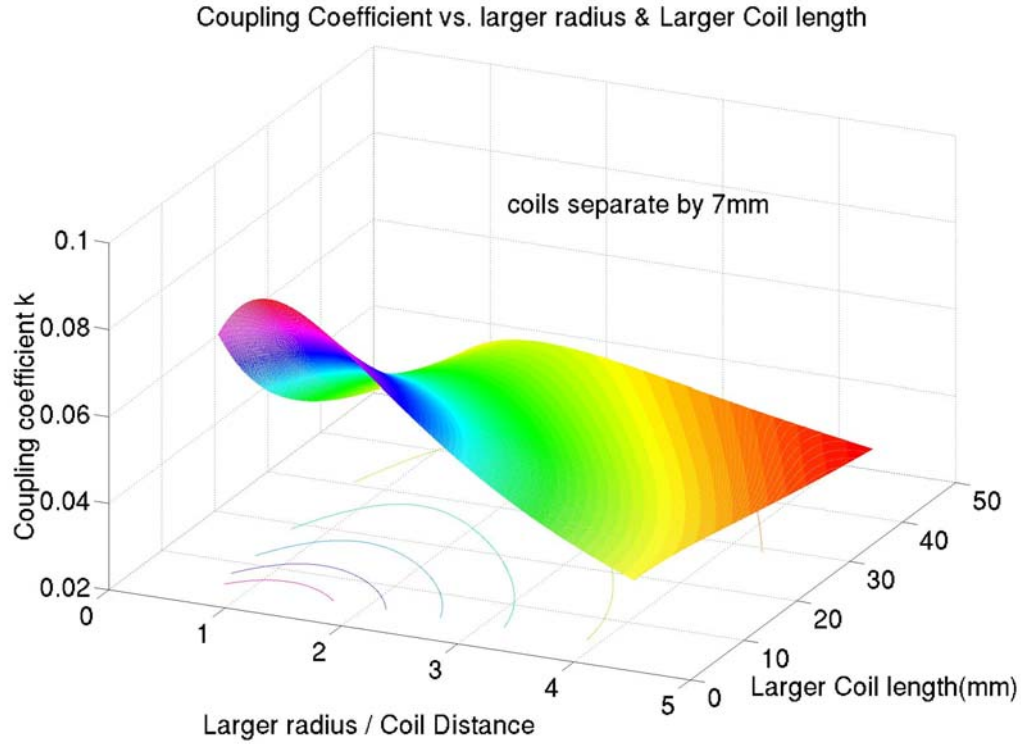


Fig. 41: The effect of the primary coil configuration on the coupling coefficient (separation is 7mm)

The above simulations are for air core coils. If a ferrite core is used, the flux leakage will be reduced and the magnetic flux density will be enhanced, so better performance can be expected. In summary, the design principles for transmitter and receiver coils are tabulated in Table 5.

|  | *Transmitter Coil* | *Receiver Coil* |
|---|---|---|
| Diameter | 1~1.5 * distance between coils | As large as possible in implant |
| Turns | Concentrate at the nearest edge to Receiver coil. Class-E PA can drive | As many as possible in implant |
| Core | Ferrite core | Ferrite core if bio-compatible |
| Coils' separation distance | As minimum as possible | |

Table 5: Coil design principles

---

[6] C.M. Zierhofer, E.S. Hochmair, "Geometric Approach for Coupling Enhancement of Magnetically Coupled Coils", *IEEE Transactions on Biomedical Engineering, Vol. 43, No. 7, July 1996*

## 6.2 On-chip Active Transmitter

*1) Design and simulation of on-chip transmitter*

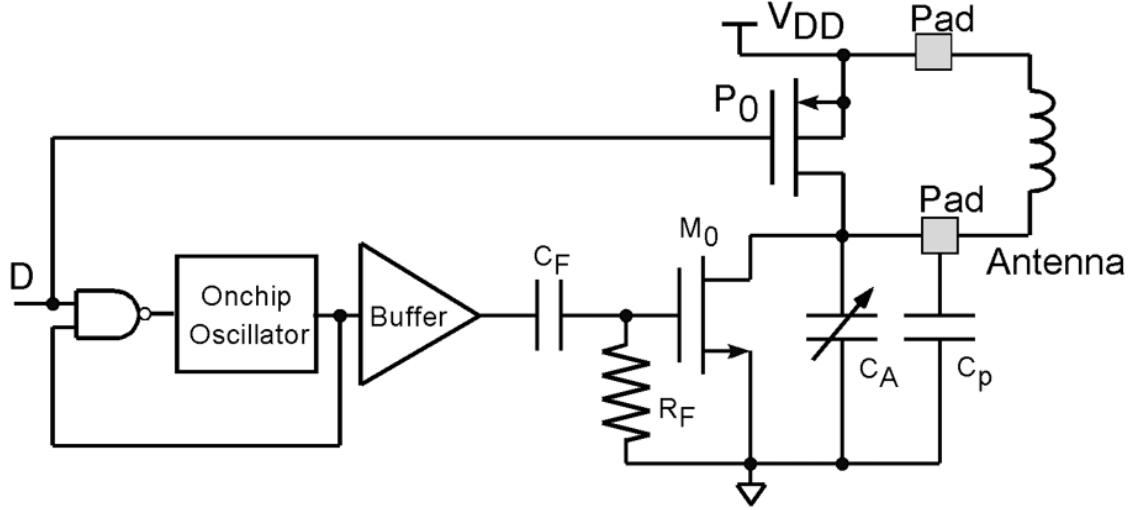An on-chip active transmitter was designed as shown in Fig. 42.



Fig. 42:  Schematic of an on-chip active transmitter

When the modulation signal D is high, the on-chip oscillator starts oscillation.  The output sinusoid is buffered and fed to the gate of M0 through a high-pass filter, composed of $C_F$ and $R_F$.  Antenna $L_A$, tuning capacitor $C_A$, pad parasitic capacitance $C_p$ and Transistor $M_0$ form a Class-C narrow band amplifier to drive sinusoid current through the small loop antenna.  When D is low, on-chip oscillator is shut off, and $P_0$ is turned on to accelerate damping at the drain of $M_0$. Note that $P_0$ is cut off and does not affect the circuit when D is high.  The small loop antenna is a 10-turn coil with diameter of 10mm.  The measured $L_A$ is 2.9µH, the series resistance is 1.5Ω and Q is 12.1, all at 1MHz, which is the maximum measurement frequency of the HP 4284A.

Our nominal working frequency is 100MHz. Because of skin effect, the ohmic resistance of the antenna increases with frequency. The ohmic resistance[7] of the small loop antenna is as following if $\phi >> \delta$,

$$R_{loss} = \frac{2N \cdot r}{\phi \cdot \delta \cdot \sigma}$$

where $\phi$ is the diameter of the wire, $\sigma$ is the conductivity of the wire material, N is the number of turns, and r is the radius of the loop.   $\delta$, the skin depth of the wire, was shown to be

---

[7] Balanis, Constantine A., "Antenna theory, analysis and design", *New York: Wiley, 1997.*

$$\delta = \frac{1}{\sqrt{\pi \cdot f \cdot \mu_0 \cdot \sigma}}$$

where f is the frequency, $\mu_0$ is the permeability of vacuum. In this case, $\delta$=6.6μm, so $\phi$>>$\delta$ holds. Consequently,

$$R_{loss} \propto \frac{N \cdot r \cdot \sqrt{f}}{\phi}$$

So it is expected that the antenna's parasitic resistance is 15Ω at 100MHz, while the inductance is relatively constant from 1M to 100MHz.

Due to the narrow bandeidth of the amplifier and high overdrive voltage at the gate of $M_0$, the waveform is approximately sinusoidal at 100MHz with an amplitude of $V_{DD}$ and DC of $V_{DD}$. The current amplitude through $L_A$ is then

$$I_L = \frac{V_{DD}}{\sqrt{(\omega L_A)^2 + R^2_{loss}}}$$

For the fabricated loop antenna, $\omega L_A$=1822Ω>>$R_{loss}$=15Ω, thus

$$I_L \cong \frac{V_{DD}}{\omega L_A}$$

If $V_{DD}$=3.3V, $I_L$≅1.8mA(0 to peak).

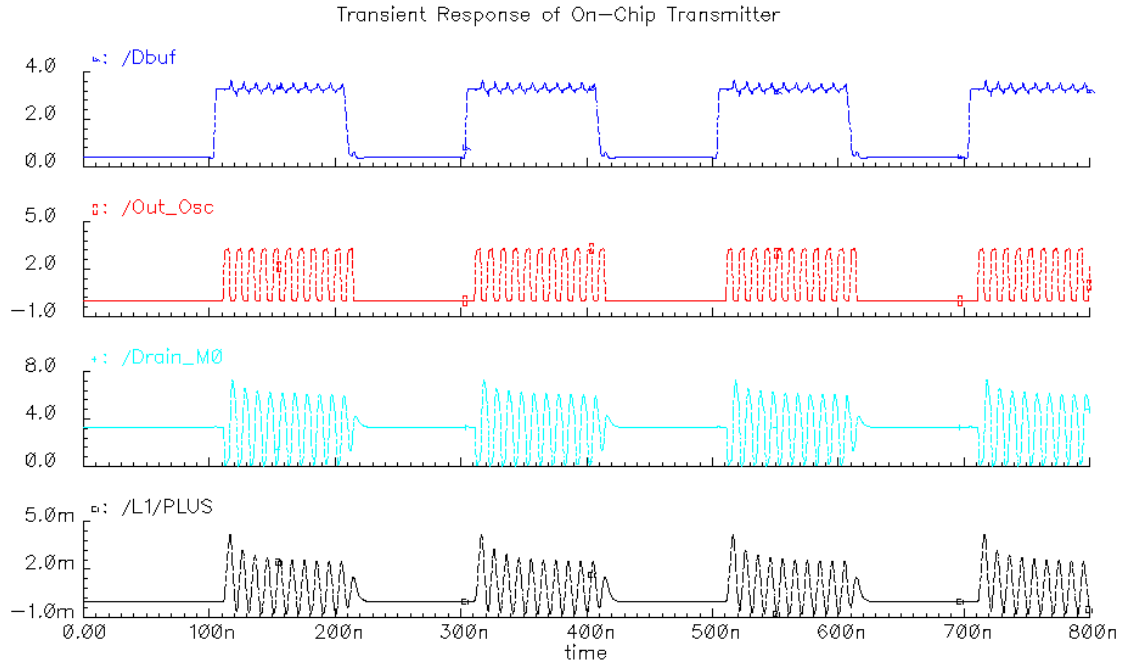This matches the simulation, where $V_{DD}$=3.3V shown in Fig. 43.



Fig. 43: Simulation results of the on-chip transmitter working in OOK

In the simulation, a 101.2MHz carrier is modulated by data with a 10MHz bit rate. The modulation scheme is On-Off-Keying (OOK). The first waveform is the buffered data and the second is the output of the oscillator. The drain voltage is illustrated in the $3^{rd}$ panel and inductor current is shown in panel 4. The drain voltage is 6.2V(p-p), and $I_L$ is 3.3mA (p-p), supporting theoretical analysis. Because of the function of $P_0$, the damping is very fast after D goes low. The average power consumption of oscillator is 58μW, and the power consumption of the class-C power amplifier and other buffers is 1.63mW.

*2) Frequency Allocation for Data Transmission*

The FCC (Federal Communication Commission) has rules and regulations that govern unlicensed use of radio spectrum. Part 15 and part 18 of title 47 of the FCC code are important for unlicensed uses for Industrial, Scientific and Medical (ISM) equipments[8]. The FCC has authorized some bands for unlicensed use in bio-telemetry and ISM equipment. The information of concern is summarized in Table 6.

| Frequency (MHz) | Bandwidth (kHz) | Field strength limit | Out of band requirements |
|---|---|---|---|
| 88-108 (FCC15.239) | 200 | 250mV/m @3m | 150mV/m @3m |
| 174-216 (FCC 15.241) | 200 | 1500mV/m @3m | 150mV/m @3m |
| 902-928 (FCC 18.301) | 915 ± 13MHz | Unlimited (FCC 18.305(a)) | 15μV/m @300m (FCC 18.305(b)) |

Table 6: FCC Frequency Allocation for Bio-telemetry and ISM equipment

In designing the on-chip transmitter, the nominal frequency is 100MHz. Because of the low power consumption of the transmitter, the field strength is far below the limit.

## 7. Conclusions

During the past quarter, research has moved forward in a number of areas. We are using immunocytochemical methods to study the sheath that forms around chronic recording electrodes and have identified two or three cellular components to this envelope. The inner layer is made up of epithelial cells, followed by reactive glia (astrocytes). A third component, neuronal processes, is less consistently present. Understanding these components should help us develop probes that are able to record consistently over much longer periods of time. We are also continuing to explore the use of liquid-crystal polymer (LCP) for the formation of flexible microcables for in-vivo use. The cables under test are 8cm long. Working with Dr. David Edell, we have insulated these cables with silicone and are soak testing the probes in-vitro. After more than three months, the cables are still exhibiting very high resistances against site-site leakage.

---

[8] FCC Part-15 Rules: Unlicensed RF Devices. FCC Part 18: ISM Equipment

Both trench-refill boron-diffusion-based probe technology and silicon-on-insulator approaches are being explored as possible alternatives to the present boron-diffused process for probe fabrication. Although no substantial performance advantages associated with the new processes are seen at this time, probes are being fabricated with both approaches to ensure that the most appropriate approach to probe fabrication is being pursued.

Active probes are being used in-vivo for current source density measurements by Dr. Gyorgy Buzsaki at Rutgers University. The 12-16-site buffered active probes have shown much superior performance with regard to immunity from motion artifact as compared to passive probes. They also eliminate the need for a headstage, simplifying the capture of multi-channel recordings. Sixty-four-site non-multiplexed probes (Pia-2B) are also being used to record from hippocampal single units with very good results. Multiplexed 64-site active probes (Pia-2) are being used in-vivo at Michigan, where software is being developed to allow multiplexed data acquisition and use of the front-end selector. The capacitively-coupled amplifiers used on these probes provide a per-channel gain of 100 and a bandwidth from <10Hz to >40kHz. The amplifiers provide a stable DC baseline and freedom from optical offsets. We are moving toward completion of a platform-mounted signal processing chip that will allow the recorded spikes to be digitized and then passed to the external world, eliminating the considerable bandwidth that would otherwise be used in transmitting below-threshold noise. A 5b analog-to-digital converter is being designed as part of the processing chip. We expect this chip to be fabricated during the coming term using the MOSIS foundry.

Finally, we have designed an external transmitter to provide power and command signals to the implanted probes. This circuitry was fully implemented and was used to provide data using a 4MHz carrier. Data rates were as high as 60kbps. An active on-chip transmitter was also designed for use on the platform. This transmitter is designed to work at 100MHz with a bit rate of 10MHz. Power consumption levels for the transmitter are about 2mW.